JEM

Article

Targeting IRF3 as a YAP agonist therapy against gastric cancer

Shi Jiao,[1]* Jingmin Guan,[1]* Min Chen,[1] Wenjia Wang,[1] Chuanchuan Li,[1] Yugong Wang,[2,4] Yunfeng Cheng,[3] and Zhaocai Zhou[1,2,4]

[1]State Key Laboratory of Cell Biology, CAS Center for Excellence in Molecular Cell Science, Shanghai Institute of Biochemistry and Cell Biology, Shanghai Institutes for Biological Sciences, Chinese Academy of Sciences, Shanghai, China
[2]School of Life Science and Technology, ShanghaiTech University, Shanghai, China
[3]Department of Hematology and Institute of Clinical Science, Zhongshan Hospital, Fudan University, Shanghai, China
[4]University of Chinese Academy of Sciences, Beijing, China

The Journal of Experimental Medicine

The Hippo pathway plays a vital role in tissue homeostasis and tumorigenesis. The transcription factor IRF3 is essential for innate antiviral immunity. In this study, we discovered IRF3 as an agonist of Yes-associated protein (YAP). The expression of IRF3 is positively correlated with that of YAP and its target genes in gastric cancer; the expression of both IRF3 and YAP is up-regulated and prognosticates patient survival. IRF3 interacts with both YAP and TEAD4 in the nucleus to enhance their interaction, promoting nuclear translocation and activation of YAP. IRF3 and YAP–TEAD4 are associated genome-wide to cobind and coregulate many target genes of the Hippo pathway. Overexpression of active IRF3 increased, but depletion of IRF3 reduced, the occupancy of YAP on the target genes. Knockdown or pharmacological targeting of IRF3 by Amlexanox, a drug used clinically for antiinflammatory treatment, inhibits gastric tumor growth in a YAP-dependent manner. Collectively, our study identifies IRF3 as a positive regulator for YAP, highlighting a new therapeutic target against YAP-driven cancers.

INTRODUCTION

Tumor development usually involves the dysregulation of multiple signaling pathways. For example, the evolutionarily conserved Hippo and Wnt pathways are both frequently disturbed in gastrointestinal carcinoma (Pan, 2010; Deitrick and Pruitt, 2016; Hong et al., 2016; Bahrami et al., 2017). Hippo signaling has been shown to control organ size and tissue homeostasis through its regulation of cell proliferation and apoptosis (Goulev et al., 2008; Wu et al., 2008; Zhang et al., 2008a; Zhao et al., 2008). Yes-associated protein (YAP) is a major downstream transcription coactivator of the Hippo pathway. The first of two layers of YAP inhibition occurs in the cytosol when YAP is phosphorylated by the upstream kinase cascade MST1/2-LATS1/2 (Huang et al., 2005; Zhao et al., 2007; Halder and Johnson, 2011). Once dephosphorylated, YAP enters the nucleus and binds the transcription factor TEAD4 to control the expression of its target genes (Wu et al., 2008; Zhao et al., 2008; Shi et al., 2017). The second layer of YAP inhibition occurs once the protein has entered the nucleus: VGLL4 antagonizes YAP activity by direct competition for binding TEAD4 (Koontz et al., 2013; Jiao et al., 2014, 2017). However, the mechanisms underlying the nuclear translocation and activation of YAP remain poorly understood, especially when viewed in comparison to the detailed knowledge about the mechanisms of YAP deactivation. YAP typically receives attention as an oncoprotein; elevated expression and nuclear localization of YAP has been associated with various cancers (Harvey and Tapon, 2007; Zeng and Hong, 2008; Pan, 2010; Zhao et al., 2010), and YAP is increasingly being recognized as a promising therapeutic target (Huang et al., 2005; Harvey and Tapon, 2007; Zhao et al., 2007, 2010; Zeng and Hong, 2008; Pan, 2010). Despite this research interest, studies of specific YAP inhibitors and their potential therapeutic use in treating cancers remain very limited; the only ones are confined to small-molecule inhibitors (Liu-Chittenden et al., 2012).

Interferon regulator factor 3 (IRF3) is a well-characterized signaling mediator/transcription factor that is essential for innate antiviral response. In host cells, viral DNA and RNA can be sensed by TLRs on endosomes or cytoplasmic receptors such as retinoic acid–inducible gene I (RIG-I) and stimulator of interferon genes protein (STING; Akira et al., 2006; O'Neill and Bowie, 2010). Binding of viral DNA and RNA to these receptors triggers signal transduction through adaptor molecules such as TIR domain–containing adapter molecule 1 or 2, mitochondrial antiviral-signaling protein (MAVS), and cyclic GMP–AMP synthase, leading to activation of the kinases TANK-binding kinase 1 (TBK1) and/or inhibitor of nuclear factor-κB kinase subunit ε (IKKε), which subsequently phosphorylate and activate IRF3 (Fitzgerald et al., 2003; Sharma et al., 2003). Activated IRF3 dimerizes and enters the nucleus to regulate both type I interferon and interferon-stimulated genes (Shinobu et al., 2002). Despite the fact that danger sig-

*S. Jiao and J. Guan contributed equally to this paper.

Correspondence to Zhaocai Zhou: zczhou@sibcb.ac.cn; Shi Jiao: jiaoshi@sibcb.ac.cn

The Rockefeller University Press
J. Exp. Med. 2018 Vol. 215 No. 2 699–718
https://doi.org/10.1084/jem.20171116

nals of self-origin are also known to activate IRF3, whether and how IRF3 functions in tumorigenesis remains unknown.

Recently, we and others have discovered a natural antagonist of YAP, namely vestigial-like family member 4 (VGLL4), as a tumor suppressor in gastric and colon cancers (Koontz et al., 2013; Jiao et al., 2014, 2017; Zhang et al., 2014). In this study, we report the identification of IRF3 as an agonist of YAP, uncovering IRF3 as a therapeutic target in gastric cancer (GC). IRF3 binds both YAP and TEAD4 to form a complex, leading to nuclear retention and activation of YAP. IRF3 and YAP are associated with each other genome-wide to co-occupy and thereby coregulate many YAP–TEAD4 target genes. We show that knockdown or pharmacological targeting of IRF3 inhibits GC growth in a YAP-dependent manner. Moreover, IRF3 is up-regulated and positively correlates with YAP hyperactivation in GC, and the increased expression of both IRF3 and YAP is negatively associated with patient survival. Thus, our study not only reveals a mechanism of YAP nuclear translocation and activation, but also highlights the potential clinical importance of targeting IRF3 as a YAP agonist.

RESULTS

Viral infection triggers YAP activation

To test whether cytosolic/viral nucleic acid sensing and type I interferon signaling affect Hippo signaling, we used a luciferase reporter assay to examine whether YAP-induced transactivation of TEAD4 could be stimulated by viral infection. To our surprise, treatment of 293FT cells with polyinosinic-polycytidylic acid (poly(I:C)) or poly(deoxyadenylic-thymidylic) acid (poly(dA:dT)), which mimic viral infection, substantially enhanced YAP-induced TEAD4 reporter activity as compared with the PBS-treated control group (Fig. 1 A). Similarly, YAP-induced TEAD4 transactivation was significantly enhanced in cells infected by various viruses, including Sendai virus (SeV), vesicular stomatitis virus (VSV), and hepatitis C virus (HCV; Fig. 1 A). Interestingly, this phenomenon was particularly prominent in the case of HCV, a major etiologic agent of hepatocellular carcinoma. Consistent with these results, the expression of YAP target genes *CTGF* and *CYR61* was greatly elevated in cells treated with poly(I:C) or poly(dA:dT) and peaked at 48 h after treatment (Fig. 1 B). Moreover, knockdown of YAP/TAZ largely diminished poly(I:C)- or poly(dA:dT)-induced up-regulation of *CTGF* and *CYR61* (Fig. 1 B). Together, these observations suggest that antiviral innate immune response activates YAP–TEAD4 and the transcription of downstream target genes.

Subsequent Western blotting analysis showed that either treatment with poly(I:C)/poly(dA:dT) or viral infection triggered phosphorylation (S396) and activation of IRF3, which is a hallmark of type I interferon immune response (Fig. 1 C). During this process, phosphorylation (S127) of YAP was significantly decreased, indicative of enhanced activation of YAP (Fig. 1 C). Meanwhile, phosphorylation of MOB1, a substrate of MST1/2 (Hippo) kinase, was not significantly changed (Fig. S1 A). Consistent with this observation, structured illumination microscopy (SIM) showed that poly(I:C)/poly(dA:dT) treatment or SeV infection clearly enhanced the nuclear translocation of YAP (Fig. 1 D).

Next, we performed RNA-seq whole-transcriptome analysis in HGC-27, a human GC cell line with hyperactivation of YAP (Jiao et al., 2014). In cells infected with SeV for 48 h, a total of 1,458 genes were altered compared with PBS-treated cells, with 1,168 genes up-regulated and 290 genes down-regulated (Table S1). Further gene set enrichment analysis (GSEA) demonstrated a global transcriptome change in SeV-infected cells, with a significant positive enrichment of YAP target genes identified in three independent studies (Zhao et al., 2008; Zhang et al., 2009; Zanconato et al., 2015; Figs. 1 E and S1 B and Tables S2, S3, and S4). Collectively, these observations indicate that viral infection facilitates nuclear enrichment and activation of YAP.

IRF3 antiviral signaling activates YAP

The RIG-I–MAVS and STING–cGAS signaling pathways are well known for their roles in detecting cytosolic viral RNA and DNA, respectively. These two pathways share the same downstream kinase (TBK1) and transcription factor (IRF3). Because both poly(I:C) and poly(dA:dT) can stimulate the activity of YAP, we assessed a potential regulatory effect of the RIG-I–MAVS and STING–cGAS pathways on the activation of YAP. 293FT cells were transfected with the TEAD4 luciferase reporter and various upstream components of the IRF3-mediated antiviral signaling axis, including RIG-I, MAVS, STING, TBK1, and IRF3(5D), a mutant that mimics phosphorylation of IRF3 and thus endows constitutive IRF3 activity (Lin et al., 1998; Servant et al., 2001; Yoneyama et al., 2002). Similar to the results for treatment with poly(I:C) and poly(dA:dT), overexpression of these IRF3-activating molecules substantially enhanced YAP-induced TEAD4 reporter activity (Fig. 2 A). Meanwhile, the transcription of the YAP target gene *CTGF* was greatly increased in cells overexpressing these molecules (Fig. 2 B). Consistent with these observations, SIM imaging showed that overexpression of MAVS, STI NG, or IRF3 (especially its active form, IRF3(5D)), strongly promoted the nuclear translocation of YAP (Figs. 2 C and S1 C). Together, these results suggest that IRF3 antiviral signaling promotes YAP activation.

To further confirm the promoting effect of IRF3 on the activation of YAP, we depleted MAVS, STING, or IRF3 using specific siRNAs in HGC-27 cells. In contrast to the observations for overexpression, knockdown of MAVS, STI NG, or IRF3 significantly decreased the nuclear localization of YAP but increased the extent of its cytosolic localization (Fig. 2 D). Comparable results were also obtained in 293FT cells (Fig. S1 D). Moreover, overexpression of IRF3, in particular IRF3(5D), significantly decreased YAP phosphorylation at S127 (Fig. 2 E), whereas knockdown of IRF3 increased such phosphorylation (Fig. 2 F). Consistent with these observations, SIM imaging showed that depletion of IRF3 appar-

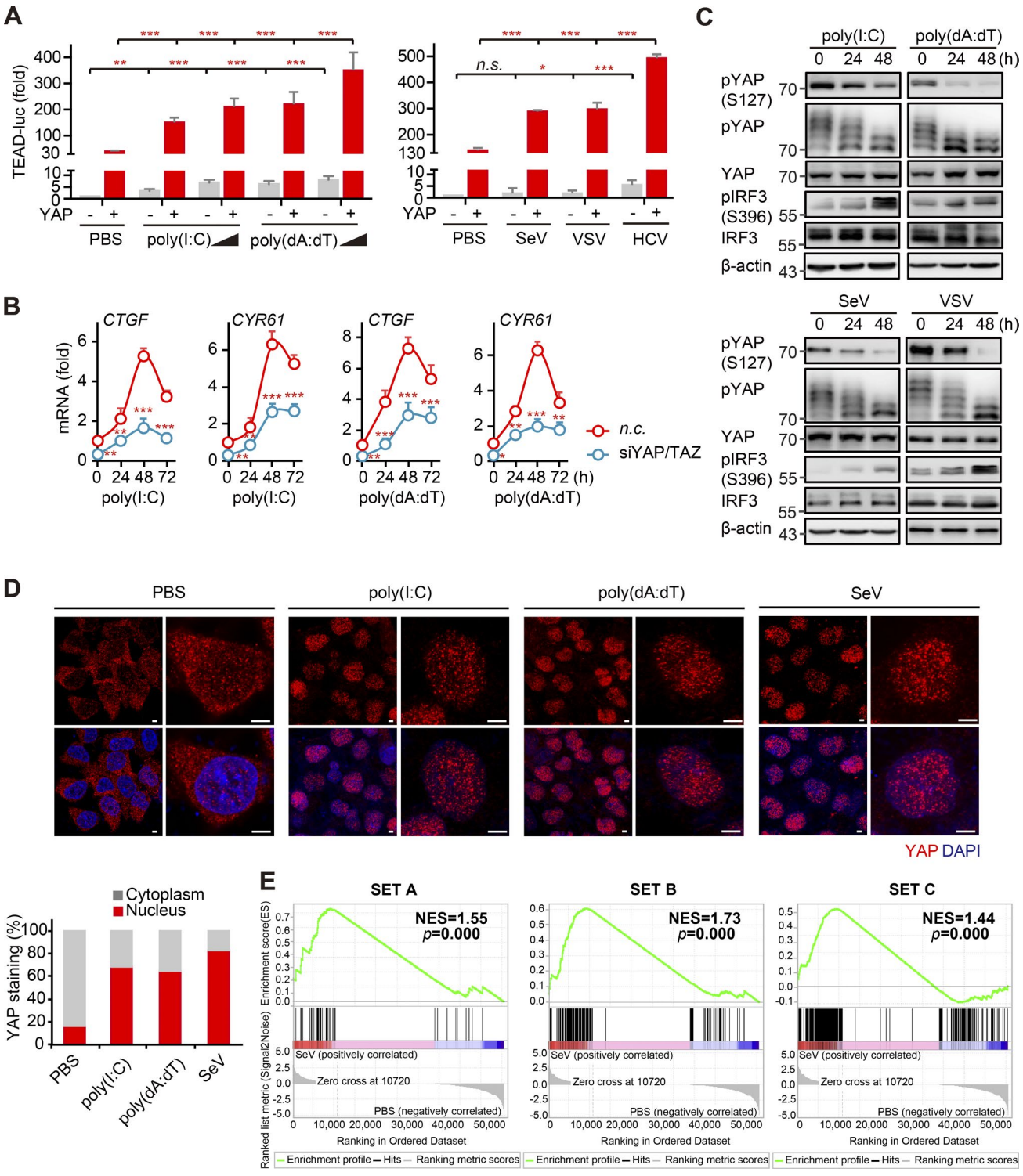

Figure 1. **Viral infection induces YAP activation. (A)** Luciferase activity of TEAD promoter in YAP-overexpressing cells after poly(I:C)/poly(dA:dT) stimulation or virus infection. HEK293FT cells were transfected with empty vector or Flag-YAP plasmid, together with TEAD-luciferase reporter, and renilla luciferase reporter for 24 h. Then, cells at 80% confluence was transfected with 0.5 or 1 µg/ml poly(I:C)/poly(dA:dT) or infected with SeV (MOI 1), VSV (MOI 0.1), or HCV (MOI 0.1) for 0 to ~48 h, and subsequently the luciferase assay was performed. **(B)** Transcriptional levels of *CTGF* and *CYR61* in YAP/TAZ-depleted cells after transfection with poly(I:C)/poly(dA:dT). Cells (70% confluence) were transfected with 1 µg/ml poly(I:C)/poly(dA:dT) for the indicated times (~0–72 h), and then real-time PCR was performed. **(C)** Immunoblotting analysis of the protein levels of YAP(S127), pYAP, YAP, pIRF3(S396), and IRF3 in HEK293FT cells after nucleic acids/virus treatment. When HEK293FT cells reached ~70% confluence, they were transfected with 1 µg/ml poly(I:C)/poly(dA:dT) or infected

ently diminished the nuclear enrichment of YAP in HGC-27 cells (Fig. 2 G). Moreover, knockdown of MAVS, STING, or IRF3 in HGC-27 cells greatly reduced the mRNA levels of YAP target genes *CTGF*, *CYR61*, and *AXL* (Figs. 2 H and S1 E). Collectively, these results indicate that IRF3 promotes nuclear retention and activation of YAP.

IRF3 binds both YAP and TEAD4 to form a complex in the nucleus

To dissect the mechanism through which IRF3 activates YAP, we examined a potential physical interaction between IRF3 and YAP. Coimmunoprecipitation (coIP) assays showed that IRF3 can associate with YAP but not LATS1 (Fig. S2 A). Furthermore, endogenous YAP interacts with endogenous IRF3, and this interaction was enhanced by treatment with poly(I:C) or poly(dA:dT), suggesting that the activation of IRF3 facilitates its interaction with YAP (Fig. 3 A). Moreover, IRF3(5D) had a much stronger interaction with YAP than did WT IRF3 (Fig. 3 B). Similarly, YAP(S127A), a dephosphorylation-mimicking mutant (Pan, 2010; Hong et al., 2016; Meng et al., 2016b), had a stronger interaction with IRF3 than did WT YAP (Fig. 3 B). Subsequent domain mapping showed that the N-terminal DNA-binding domain (amino acids 1–191) of IRF3 interacts specifically with the N-terminal region of YAP (amino acids 1–290) that contains both the TEAD-binding domain and the tandem WW domains (Fig. S2, B and C). Further pull-down assays using purified recombinant proteins revealed that the interaction between IRF3 and YAP is a direct one (Fig. S2 D). These experiments demonstrate that IRF3 interacts with YAP, and such interaction is enhanced by poly(I:C)/poly(dA:dT) treatment and thus activation of IRF3.

Because it is also known that nuclear YAP binds to the transcription factor TEAD4 for gene regulation and that YAP–TEAD4 interaction helps to retain YAP in the nucleus, we next explored the potential effect of IRF3 on the interaction between YAP and TEAD4. Our coIP assay showed that IRF3(5D) dramatically enhanced the association of YAP with TEAD4 (Fig. 3 C). On the contrary, the amount of YAP that interacts with LATS1 was significantly reduced by overexpression of IRF3, particularly its 5D mutant (Fig. S2 E). Given that IRF3 can directly bind to YAP, we further examined whether IRF3 may also interact with TEAD4, thereby promoting the association between YAP and TEAD4. Indeed, our coIP assay showed that FLAG-tagged TEAD4 interacts readily with HA-tagged IRF3, especially its 5D mutant (Fig. 3 D). This result was then confirmed by immunofluorescence assay showing a strong signal for colocalization of IRF3 and TEAD4 (Fig. 3 E). Further pull-down assays using in vitro translated proteins indicated that the interaction between IRF3 and TEAD4 is also direct (Fig. 3 F). To further confirm these observations about the direct interaction of IRF3 and TEAD4 and rule out the possibility of DNA-mediated association between IRF3 and TEAD4, we performed endogenous IP with DNase. We found that endogenous IRF3 can interact with endogenous TEAD4 even after DNase digestion, and such interaction was enhanced by SeV infection (Fig. 3 G). Consistent with this result, gel filtration chromatography showed that IRF3, YAP, and TEAD4 could be partially coeluted in the lysate of cells treated with poly(I:C) (Fig. S2 F). Collectively, these results indicate that IRF3 directly associates with both YAP and TEAD4 to from a complex in the nucleus; as such, IRF3 retains YAP in the nucleus and promotes its association with TEAD4 (Fig. 3 H).

Genome-wide association between IRF3 and YAP–TEAD4

To further investigate the regulatory role of IRF3 on YAP–TEAD4 activation and gene transcription, we assessed the genome-wide association between IRF3 and YAP–TEAD4. To this end, we performed chromatin immunoprecipitation (ChIP) assays with YAP, TEAD4, and IRF3 antibodies in HGC-27 cells, followed by ChIP-seq (Fig. 4 A). Analysis of the distribution of YAP-, TEAD4-, or IRF3-binding sites relative to genes annotated in the human genome revealed that only a minute fraction of peaks mapped close (<1 kb) to transcription start sites (TSSs), whereas most peaks were located farther than 10 kb from the closest TSS (Fig. 4 B). A total of 6,277 peaks were identified by both YAP and IRF3 antibodies, whereas 7,012 peaks were identified by both TEAD4 and IRF3 antibodies (Fig. 4 C and Table S5). YAP and TEAD4 were present in 61% (5,275/8,715) of the peaks identified by the IRF3 antibody, and most of these shared binding sites are located on active enhancers, indicating a genome-wide association between IRF3 and YAP/TEAD4 (Fig. 4 C). In support of this notion, the signal of IRF3 peaks is positively correlated with that of YAP/TEAD4 peaks (Fig. 4 D and Table S6). YAP/TEAD4/IRF3-bound regions include the promoters of previously established YAP/TEAD direct targets (CTGF, CYR61, AXL), and highly similar pat-

with SeV (MOI 1)/VSV (MOI 0.1) for the indicated duration of time (0, 24, or 48 h). Cell lysates were prepared and subjected to immunoblotting for the indicated proteins and phosphorylation. Phos-tag denotes phos-tag gel used to resolve phosphorylated YAP based on mobility shift. Molecular mass is indicated in kilodaltons. **(D)** Localization of YAP in cells with or without nucleic acids/virus treatment. After nucleic acids/virus treatment for 48 h, cells were cultured sparsely or to confluence. YAP was then stained with anti-YAP antibody. Bars, 10 µm. **(E)** GSEA analysis showing significant positive enrichment of three sets of YAP targets genes in SeV-infected HGC-27 cells by RNA-seq. HGC-27 cells (~80% confluence) were infected with SeV (MOI 1) for 48 h. Total RNA was extracted, and RNA-seq was subsequently performed. At least two independent experiments were performed for all data. Two biological replicates were used for RNA-seq. For bar figures and curve figures, data are presented as means ± SD. Unpaired Student's *t* tests were used for comparing two variables. One-way ANOVA was used for multiple variables comparison. *, $P < 0.05$; **, $P < 0.01$; ***, $P < 0.001$; *n.s.*, no significance in comparison with control group.

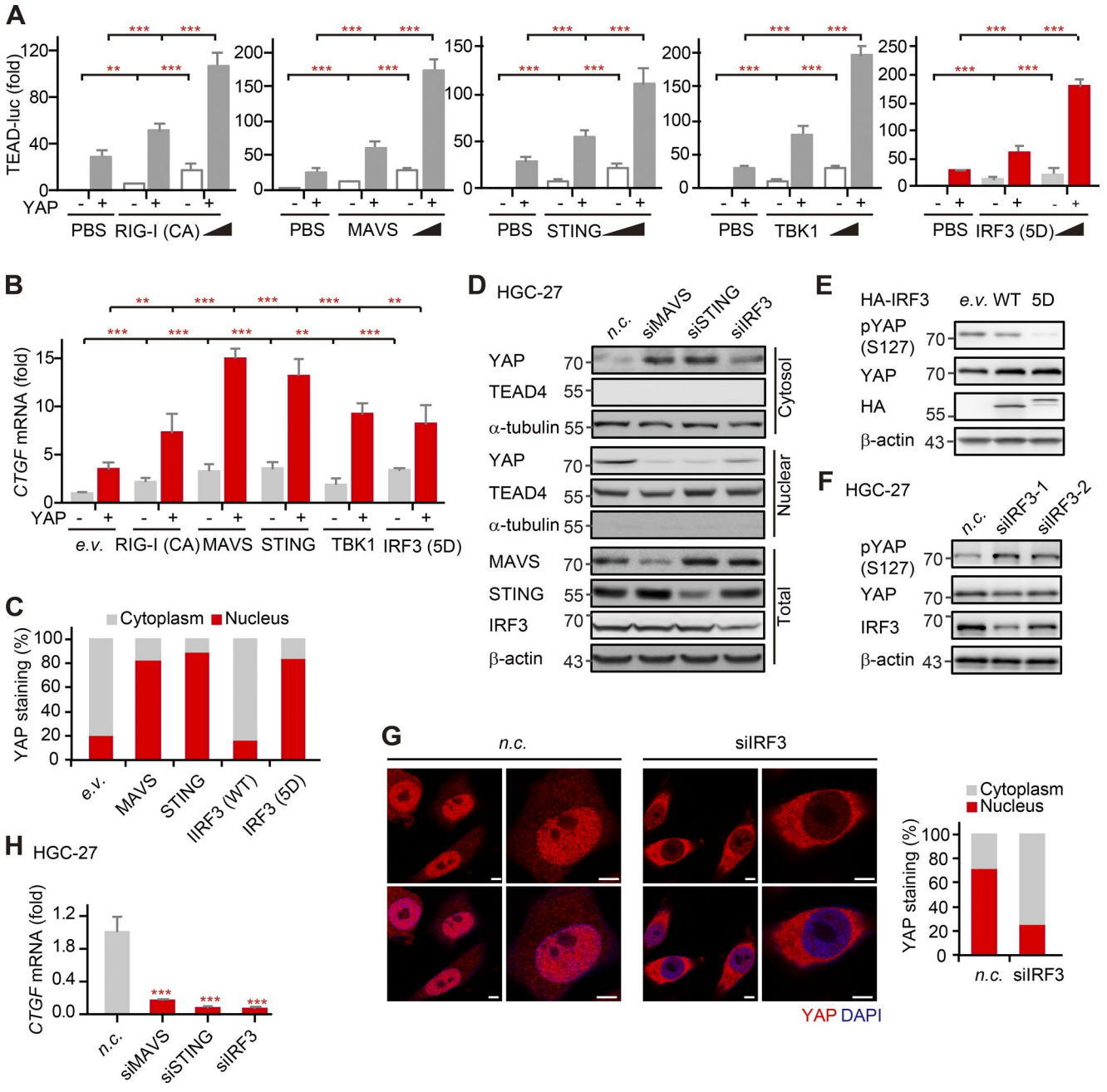

Figure 2. **IRF3–mediated antiviral signaling regulates YAP activity. (A)** Transactivity of TEAD4 promoter and transcription of *CTGF* in YAP-overexpressing HEK293FT cells after transfection with the CARD domain of RIG-I, MAVS, STING, TBK1, or IRF3(5D). **(B)** mRNA levels of *CTGF* in YAP-overexpressing cells after transfection with the indicated plasmids. **(C)** YAP staining in cells overexpressing the indicated plasmids. **(D)** Nuclear localization of YAP in HGC-27 cells after transfection with siMAVS, siSTING, or siIRF3, respectively. **(E)** Immunoblotting analysis of the protein levels of p-YAP(S127) in HEK293FT cells transfected with the indicated plasmids. **(F)** Immunoblotting of the protein levels of pYAP(S127) in HGC-27 cells after transfection with specific IRF3 siRNAs. Molecular mass is indicated in kilodaltons. **(G)** YAP staining in IRF3-depletion cells. After transfection with IRF3 siRNAs (a mixture of siIRF3-1 and siIRF3-2) for 48 h, HGC-27 cells were seeded in 33-mm dishes to ∼20–30% confluence. YAP was then stained with anti-YAP antibody. Bars, 10 µm. **(H)** *CTGF* mRNA in cells after transfection with indicated siRNAs. At least two independent experiments were performed for all data. For bar figures, data are presented as means ± SD. Unpaired Student's *t* tests were used for comparing two variables. One-way ANOVA was used for multiple variables comparison. **, $P < 0.01$; ***, $P < 0.001$; 5D, IRF3(S396D/S398D/S402D/S405D/T404D); *e.v.*, empty vector; *n.c.*, negative control siRNA.

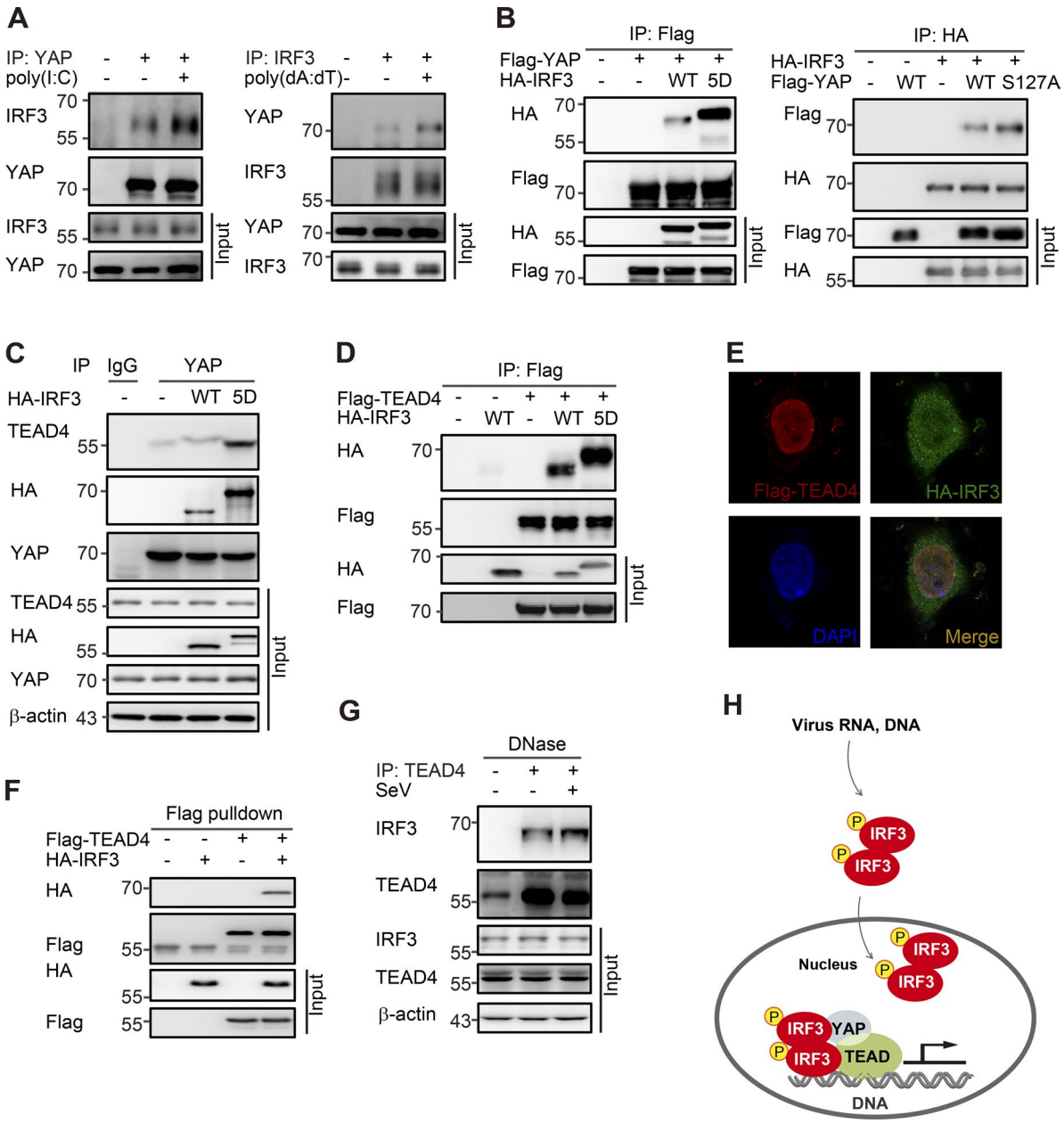

Figure 3. **IRF3 binds both YAP and TEAD4 to form a complex in the nucleus. (A)** CoIP of endogenous YAP and IRF3 in HGC-27 cells after treatment with poly(I:C) and poly(dA:dT). **(B)** CoIP analysis of WT or mutant YAP with WT or mutant IRF3. **(C)** CoIP of YAP with TEAD4 in HEK293FT cells after transfection with the indicated plasmids. **(D)** Exogenous coIP of Flag-TEAD4 with HA-IRF3 or HA-IRF3(5D). **(E)** Colocalization of Flag-TEAD4 with HA-IRF3. **(F)** Flag pull-down assay to assess the interaction of TEAD4 and IRF3. **(G)** CoIP of endogenous TEAD4 and IRF3 in SeV-infected cells with or without 10 µg/ml DNase. Molecular mass is indicated in kilodaltons. **(H)** Schematic model showing that IRF3 binds both YAP and TEAD4 to form a complex, thus retaining YAP in the nucleus. For all data, experiments were repeated two times.

terns were observed for YAP/TEAD4/IRF3 occupancy on these genes (Fig. 4 E).

To corroborate our ChIP-seq analyses, we examined the occupancy of IRF3 and YAP on specific target gene loci by ChIP assay. As expected, a group (>10) of YAP–TEAD4 target genes can be ChIP'ed by not only the YAP antibody, but also by the IRF3 antibody (Fig. S3 A). Compared with WT IRF3, the 5D mutant could better bind to *CTGF* and *CYR61* (Fig. 4 F). Moreover, the occupancy of YAP on *CTGF* and *CYR61* was greatly enhanced by overexpression of IRF3, especially IRF3(5D) (Fig. 4 G); whereas knockdown of IRF3 decreased YAP occupancy on these loci (Fig. S3 B). Furthermore, the occupancies of both YAP and IRF3 on *CTGF* promoter were significantly increased upon treatment

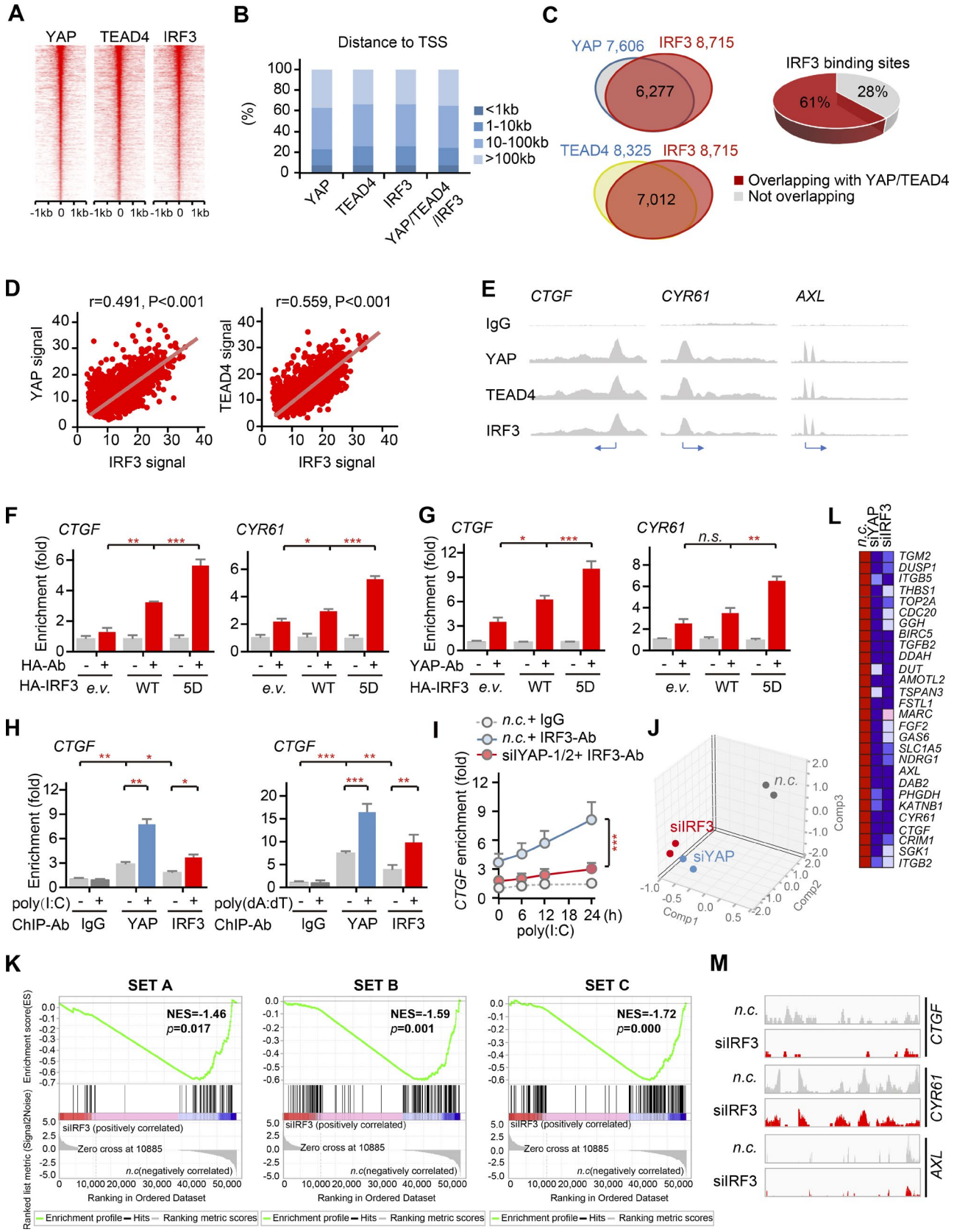
A
YAP
TEAD4
IRF3
-1kb 0 1kb
B
Distance to TSS
(%)
<1kb
1-10kb
10-100kb
>100kb
YAP
TEAD4
IRF3
YAP/TEAD4 /IRF3
C
YAP 7,606
IRF3 8,715
6,277
TEAD4 8,325
IRF3 8,715
7,012
IRF3 binding sites
61%
28%
Overlapping with YAP/TEAD4
Not overlapping
D
r=0.491, P<0.001
YAP signal
IRF3 signal
r=0.559, P<0.001
TEAD4 signal
IRF3 signal
E
CTGF
CYR61
AXL
IgG
YAP
TEAD4
IRF3
F
CTGF
CYR61
Enrichment (fold)
HA-Ab
HA-IRF3
e.v.
WT
5D
G
CTGF
CYR61
n.s.
Enrichment (fold)
YAP-Ab
HA-IRF3
e.v.
WT
5D
L
n.c.
siYAP
siIRF3
TGM2
DUSP1
ITGB5
THBS1
TOP2A
CDC20
GGH
BIRC5
TGFB2
DDAH
DUT
AMOTL2
TSPAN3
FSTL1
MARC
FGF2
GAS6
SLC1A5
NDRG1
AXL
DAB2
PHGDH
KATNB1
CYR61
CTGF
CRIM1
SGK1
ITGB2
H
CTGF
CTGF
Enrichment (fold)
poly(I:C)
ChIP-Ab
IgG
YAP
IRF3
poly(dA:dT)
ChIP-Ab
IgG
YAP
IRF3
I
n.c.+ IgG
n.c.+ IRF3-Ab
siYAP-1/2+ IRF3-Ab
CTGF enrichment (fold)
poly(I:C)
J
n.c.
siIRF3
siYAP
Comp1
Comp2
Comp3
K
SET A
SET B
SET C
NES=-1.46
p=0.017
NES=-1.59
p=0.001
NES=-1.72
p=0.000
Enrichment score(ES)
Ranked list metric (Signal2Noise)
siIRF3 (positively correlated)
Zero cross at 10885
n.c(negatively correlated)
Ranking in Ordered Dataset
Enrichment profile
Hits
Ranking metric scores
M
n.c.
siIRF3
CTGF
CYR61
AXL

with poly(I:C) or poly(dA:dT) (Fig. 4 H). Knockdown of IRF3 largely abrogated the effect of poly(I:C)-induced YAP binding to the promoter regions of *CTGF*, *CYR61,* and *AXL* (Figs. 4 I and S3 C). Because the same pair of primers corresponding to each gene were used for the ChIP assays, these results clearly indicate that IRF3 and YAP were bound to the same loci of the tested genes.

Subsequently, we performed RNA-seq whole-transcriptome analysis in HGC-27 cells transfected with siIRF3 or siYAP. After alignment to the human reference genome and normalization, we identified a total of 23,929 and 23,878 transcripts in negative control (*n.c.*) and siIRF3-treated cells, respectively. This information was used to evaluate transcriptional differences between the *n.c.* and siIRF3 groups. In total, 833 and 775 genes exhibited significant up-regulation and down-regulation, respectively, in IRF3 knockdown cells relative to their expression in control cells. These results documented an incremental transcriptional shift between *n.c.* and siIRF3 and demonstrated global transcriptome changes immediately after transfection with siIRF3 (Tables S7, S8, and S9). Primary component analysis clearly revealed a close association between the siIRF3 group and the siYAP group, both negatively correlated with the *n.c.* group (Fig. 4 J). 812 uniquely expressed transcripts were identified in both siIRF3 and siYAP groups (Fig. S3 D). In addition, GSEA revealed a significant negative enrichment of YAP target genes upon IRF3 knockdown (Fig. 4 K and Tables S2, S3, and S4). Most of the enriched YAP target genes were down-regulated in the siIRF3 group compared with the control (Fig. 4, L and M). Collectively, these results reveal genome-wide associations between IRF3 and YAP–TEAD4; and indicate that IRF3 acts as part of a YAP–TEAD4-containing transactivation complex to enhance YAP–TEAD4 occupancy on target genes and therefore coregulate their transcription.

Depletion of IRF3 inhibits YAP-driven GC growth

To explore the function of IRF3 in tumorigenesis, we examined the effect of IRF3 on the growth of several GC cell lines with various differentiation states, including HGC-27, BGC-823, and MKN-45. Previously, we observed elevated levels of YAP in HGC-27 and BGC-823 cells but low levels of YAP in MKN-45 cells (Jiao et al., 2014). Here, we first measured cell proliferation on plates and monitored anchorage-independent growth of these GC cells in soft agar. Knockdown of IRF3 by specific siRNA targeting significantly inhibited the proliferation (Fig. 5 A) and colony formation (Figs. 5 B and S4 A) of HGC-27 and BGC-823 but not MKN-45 cells, hinting at a YAP-dependent effect. Moreover, these inhibitory effects of siIRF3 in HGC-27 or BGC-823 cells were readily blocked by overexpressing an active form of YAP(S127A) (Fig. 5, C and D; and Fig. S4 B). Together, these results indicate that IRF3 positively regulates GC growth in a YAP-dependent manner.

We then performed a xenograft tumor study by injecting GC cells into the flank of BALB/cA nu/nu mice. Once palpable tumors were detected, pairs of mice were randomized and treated with lentivirus-delivered shIRF3 or scramble shRNA. We found that shIRF3 treatment substantially decreased the size and weight of tumors derived from HGC-27 and BGC-823, but not MKN-45, cells (Fig. 5, E and F). Consistently, the mRNA levels of the *CTGF* and *CYR61* were significantly down-regulated in shIRF3-treated tumors derived from HGC-27 and BGC-823 (Fig. S4 C). These observations again indicate that GC cells with high levels of YAP are more sensitive to depletion of IRF3.

Next, we assessed the therapeutic potential of targeting IRF3 in *IRF3*$^{-/-}$ mice using a gastric tumor model developed with *Helicobacter pylori* infection and cocarcinogen *N*-methyl-*N*′-nitro-*N*-nitrosoguanidine (MNNG; Jiao et al., 2014). IRF3 was first knocked out in C57BL/6 mice using CRISPR/Cas9. For gastric tumor formation, a 50-µl bacterial suspension of *H. pylori* (~10^6 CFU) was intragastrically administered once every day in drinking water containing 100 mg/ml MNNG. Consistent with our xenograft study, the number and volume of palpable tumors in the *IRF3*$^{-/-}$ mice were substantially less than those in WT mice (Fig. 5 G). These observations were further confirmed by immunohistochemical (IHC) staining of Ki67 for mice sacrificed at various time points (0, 90, and 180 d) during the course of the

Figure 4. **Genome-wide association of IRF3 with YAP and TEAD4. (A)** Heat map representing YAP, TEAD4, and IRF3 binding sites located on promoters (top) and enhancers (bottom). YAP, TEAD4, and IRF3 peaks are ranked from the strongest to weakest signal. **(B)** Absolute distance of YAP peaks (*n* = 7,606), TEAD4 peaks (*n* = 8,325), IRF3 peaks (*n* = 8,715), or overlapping YAP/TEAD4/IRF3 peaks (*n* = 6,275) to the nearest TSS. **(C)** Overlap of peaks identified with YAP, TEAD4, and IRF3 antibodies. **(D)** Linear correlation between the signal of YAP or TEAD4 and IRF3 peaks in the 6,275 shared binding sites. *r* is the coefficient of determination of the two correlations. **(E)** Representative examples of YAP/TEAD4/IRF3 binding profiles in the genome of HGC-27 cells. **(F)** ChIP assay showing IRF3 bound to the indicated genes' promoters in 293FT cells transfected with HA-IRF3 or HA-IRF3(5D). Chromatin was immunoprecipitated with the HA antibody followed by qPCR using primer pairs spanning the human CTGF or CYR61 locus. **(G)** ChIP-qPCR showing YAP binding to the promoter of indicate genes in 293FT cells transfected with WT IRF3 and its mutant. **(H)** ChIP experiment performed with YAP antibody or IRF3 antibody in cells after transfection with poly(I:C). **(I)** ChIP experiment performed with YAP antibody in IRF3-depleted HGC-27 cells. **(J)** Primary component analysis for each siRNA. n.c. (gray), siYAP (blue), and siIRF3 (red) are indicated in the 3D scatter plot. A mixture of the two siRNAs for each gene was used. **(K)** GSEA analysis showing significant negative enrichment of three sets of YAP targets genes in siIRF3 group. **(L)** Heat map indicating the YAP targets genes that are significantly down-regulated in IRF3 knockdown state. **(M)** RNA-seq reads for YAP target genes (*CTGF*, *CYR61*, and *AXL*) by using IGV browser. For all ChIP assays, results are presented as percentage immunoprecipitated over input (0.5%) and are representative of three independent experiments. *, P < 0.05; **, P < 0.01; ***, P < 0.001; *n.s.*, not significant relative to control group.

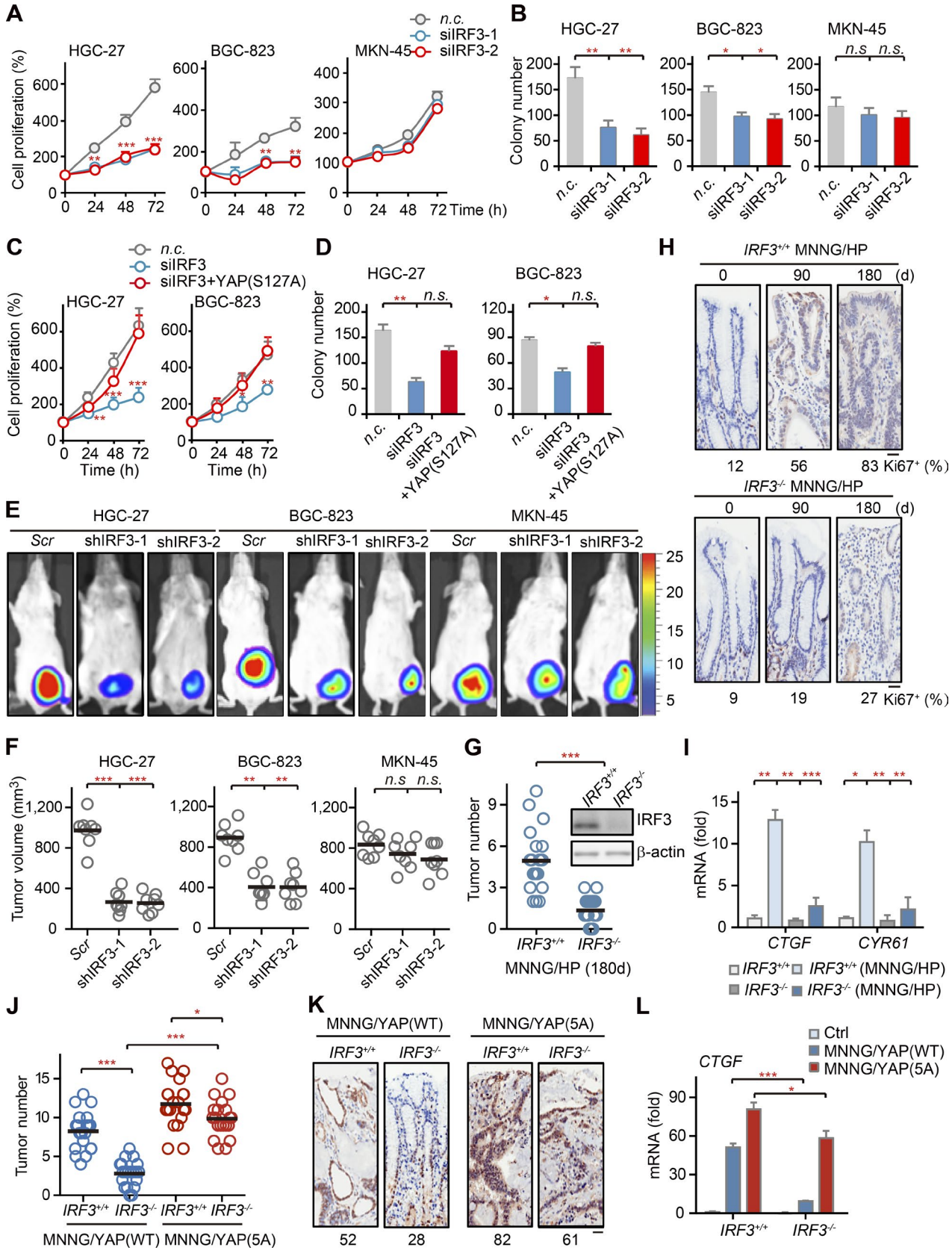
A
HGC-27
BGC-823
MKN-45
n.c.
siIRF3-1
siIRF3-2
Cell proliferation (%)
Time (h)
B
HGC-27
BGC-823
MKN-45
Colony number
n.s
C
n.c.
siIRF3
siIRF3+YAP(S127A)
Cell proliferation (%)
Time (h)
D
HGC-27
BGC-823
Colony number
n.s.
n.c.
siIRF3
siIRF3 +YAP(S127A)
H
IRF3+/+ MNNG/HP
IRF3-/- MNNG/HP
(d)
Ki67+ (%)
12
56
83
9
19
27
E
HGC-27
BGC-823
MKN-45
Scr
shIRF3-1
shIRF3-2
F
HGC-27
BGC-823
MKN-45
Tumor volume (mm3)
G
Tumor number
IRF3
β-actin
IRF3+/+
IRF3-/-
MNNG/HP (180d)
I
mRNA (fold)
CTGF
CYR61
IRF3+/+
IRF3+/+ (MNNG/HP)
IRF3-/-
IRF3-/- (MNNG/HP)
J
Tumor number
IRF3+/+
IRF3-/-
MNNG/YAP(WT)
MNNG/YAP(5A)
K
MNNG/YAP(WT)
MNNG/YAP(5A)
IRF3+/+
IRF3-/-
52
28
82
61
L
CTGF
Ctrl
MNNG/YAP(WT)
MNNG/YAP(5A)
mRNA (fold)
IRF3+/+
IRF3-/-

H. pylori–infected gastric tumor model (Fig. 5 H). Moreover, the expression of *CTGF* and *CYR61* were obviously down-regulated in *IRF3*$^{-/-}$ mice compared with WT mice during modeling GC (Fig. 5 I). Notably, both Ki67 staining and YAP target gene expression were significantly reduced in *IRF3*$^{-/-}$ mice, even before tumorigenesis (0 d; Fig. 5, H and I). Given that YAP levels are elevated in *H. pylori*–infected gastric tumor (Jiao et al., 2014), these results suggest that depletion of IRF3 inhibits YAP-driven GC growth.

Because *H. pylori* is known to drive inflammation and metaplasia, it is possible that targeting IRF3 could suppress tumor growth via the reduction of inflammation. To further determine whether the tumor-suppressive role of IRF3 depletion is cell autonomous via YAP, we used YAP instead of *H. pylori*, in combination with MNNG, for modeling GC in mice (Fig. S4 D). In this model, knockout of IRF3 also greatly suppressed GC growth (Fig. 5, J and K). However, this effect was largely diminished when we used YAP(5A), a mutant that has strong constitutive activity, for GC modeling (Fig. 5, J and K). Consistent with these observations, IRF3 knockout markedly reduced the expression of CTGF in MNNG/YAP-induced tumors, but only had a modest effect in MNNG/YAP(5A)-induced tumors (Fig. 5 L). Collectively, these results strongly indicate that depletion of IRF3 suppresses GC growth mainly through limiting YAP activity.

Pharmacological targeting IRF3 as a GC therapy

Because phosphorylation and activation of IRF3 can promote the nuclear translocation and activation of YAP, we reasoned that targeting the IRF3 upstream kinase TBK1 may decrease IRF3 activity, leading to suppression of YAP-driven GC growth. To test this possibility, we first examined the possible effect of TBK1 depletion in HGC-27 and BGC-823 cells. Like the effects of siIRF3 treatment, knockdown of TBK1 significantly inhibited the proliferation and colony formation of the GC cells, and such effects could be blocked by forced activation of YAP (Fig. S5, A and B). Next, we used the TBK1 inhibitor Amlexanox, a drug that has been used clinically as an immunomodulator to treat inflammatory diseases including recurrent aphthous ulcers (Fig. 6 A; Murray et al., 2005; Liu et al., 2006; Meng et al., 2009). Indeed, Amlexanox inhibited the expression of not only the IRF3 target gene *IFNB*, but also the YAP target gene *CTGF* (Fig. S5 C). Treatment with Amlexanox significantly inhibited, in a dose-dependent manner, the proliferation and colony formation of GC cells HGC-27 and BGC-823 but not of MKN-45 (Fig. 6, B and C; and S5 D). Moreover, these inhibitory effects of Amlexanox in the GC cells were abrogated by introducing the active form of YAP(S127) (Fig. 6, D and E).

To further evaluate the efficacy and sensitivity of Amlexanox against GC growth, we measured the half-maximal inhibitory concentration (IC_{50}) in 12 GC cell lines and four primary GC cells (ZGC-1, ZGC-2, ZGC-3, and ZGC-4), with different YAP levels (Fig. S5 E). Notably, Amlexanox significantly inhibited the viability of HGC-27 (IC_{50} 3.90 μM), MGC-803 (IC_{50} 3.2 μM), KATOIII (IC_{50} 8.7 μM), SNU-1 (IC_{50} 7.6 μM), and ZGC-1 (IC_{50} 4.3 μM) cells; moderately inhibited the viability of BGC-823 (IC_{50} 33.0 μM), SGC-7901 (IC_{50} 31.5 μM), MKN-1 (IC_{50} 12.4 μM), GES (IC_{50} 17.3 μM), and ZGC-2 (IC_{50} = 21.7 μM) cells; but only marginally inhibited the viability of NCI-N87, MKN-45, AGS, SNU-216, ZGC-3, and ZGC-4 cells (IC_{50} > 100 μM; Fig. 6 F). These observations indicate some selectivity in the effects of Amlexanox for the inhibition of tumor cell growth. In particular, we found that YAP levels tend to correlate with the sensitivity of tumor cells toward Amlexanox treatment (Figs. 6 F and S5 E). For example, HGC-27 cells (with high YAP levels) were more susceptible to Amlexanox treatment than MKN-45 cells (with low YAP levels; Figs. 6 F and S5 E). Thus, it appears that Amlexanox may specifically target tumor cells with elevated YAP expression. Indeed, overexpression of YAP sensitized MKN-45 cells (Fig. S5 F), whereas knockdown of YAP desensitized HGC-27 cells, toward Amlexanox treatment (Fig. S5 G).

Subsequent xenograft studies further confirmed that Amlexanox could, in a dose-dependent manner, inhibit the growth of gastric tumors with hyperactive YAP (HGC-27 and BGC-823); 5-fluorouracil (5-FU), a conventional drug used for chemical treatment of GC, has a similar effect (Fig. 6, G and H). The mRNA levels of *CTGF* and *CYR61* were also

Figure 5. **Targeting IRF3 inhibits GC growth. (A)** Cell proliferation of HGC27, BGC-823, and MKN45 cells after transfection with IRF3 siRNAs. **(B)** Colony formation of IRF3-depleted cells. **(C)** Cell proliferation of HGC27 and BGC-823 cells after transfection with IRF3 siRNAs (a mixture of two siRNAs) together with YAP(S127A). **(D)** Colony formation of IRF3-depleted cells after transfection with YAP(S127A). **(E)** Knockdown of endogenous IRF3 inhibited xenograft tumor growth. Mice were photographed after being killed. BALB/cA nu/nu mice (aged 4 wk) were injected with the GC cell lines (HGC-27, BGC-823, and MKN-45). Once palpable tumors were detected, pairs of mice were randomized and treated with lentivirus-delivered shIRF3 or scramble shRNA by subcutaneous injection (n = 10). **(F)** Tumor volumes for the mice from E. **(G)** Tumor numbers in WT and *IRF3*$^{-/-}$ mice after administration of *H. pylori* intragastrically with alkylating agent MNNG in drinking water. 4-wk-old *IRF3*$^{-/-}$ mice and their WT littermates were orally gavaged with 50 µl of bacterial suspension (~10^6 CFU) every day, which persisted for at least 6 mo before sacrifice. 100 mg/ml MNNG was added to the drinking water for a period of up to 2 mo. A total of 40 mice were reared, including 20 normal controls. **(H)** Ki67 staining of adenomas from G. Bar, 50 µm. **(I)** Relative mRNA levels of YAP target genes in gastric tissue from G. **(J)** Tumor numbers in WT and *IRF3*$^{-/-}$ mice after administration of YAP lentivirus intragastrically with alkylating agent MNNG in drinking water. **(K)** Ki67 staining of adenomas from J. Bar, 50 µm. **(L)** Relative mRNA levels of YAP target genes in gastric tissue from J. At least two independent experiments were performed for all data. For curve figures and bar figures, data are presented as means ± SD. Unpaired Student's t tests were used for comparing two variables. One-way ANOVA was used for multiple variables comparison. *, P < 0.05; **, P < 0.01; ***, P < 0.001; *n.s.*, no significance in comparison with control group.

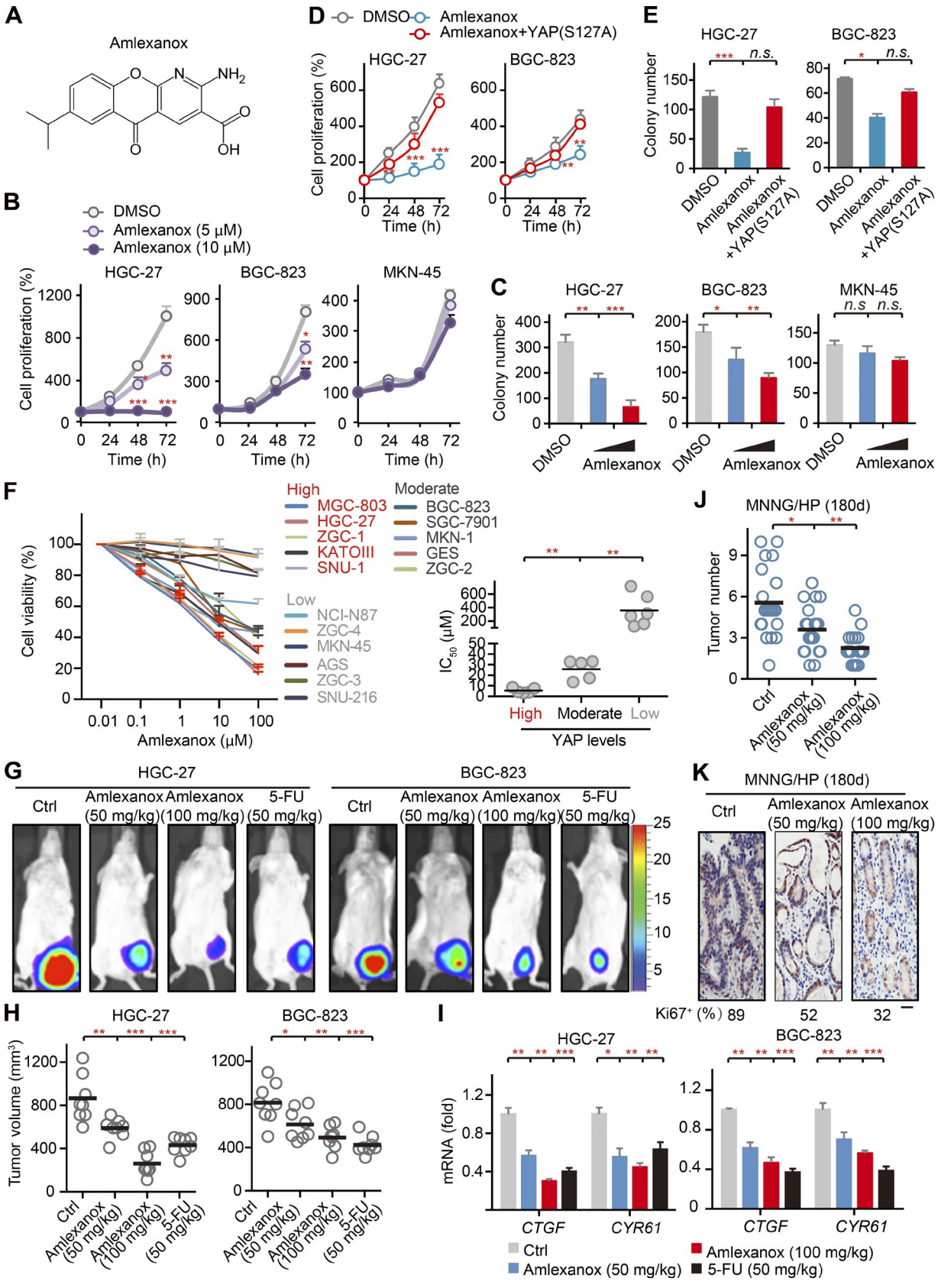
A
Amlexanox
B
DMSO
Amlexanox (5 μM)
Amlexanox (10 μM)
HGC-27
BGC-823
MKN-45
Cell proliferation (%)
Time (h)
C
Colony number
DMSO
Amlexanox
D
DMSO
Amlexanox
Amlexanox+YAP(S127A)
E
n.s.
Amlexanox +YAP(S127A)
F
High
MGC-803
HGC-27
ZGC-1
KATOIII
SNU-1
Moderate
BGC-823
SGC-7901
MKN-1
GES
ZGC-2
Low
NCI-N87
ZGC-4
MKN-45
AGS
ZGC-3
SNU-216
Cell viability (%)
Amlexanox (μM)
IC50 (μM)
YAP levels
G
Ctrl
Amlexanox (50 mg/kg)
Amlexanox (100 mg/kg)
5-FU (50 mg/kg)
H
Tumor volume (mm3)
I
mRNA (fold)
CTGF
CYR61
Ctrl
Amlexanox (50 mg/kg)
Amlexanox (100 mg/kg)
5-FU (50 mg/kg)
J
MNNG/HP (180d)
Tumor number
K
Ki67+ (%) 89
52
32

decreased in tumor tissues treated with Amlexanox (Fig. 6 I). Consistent with these observations, Amlexanox treatment also reduced the tumor number (Fig. 6 J) and the extent of Ki67 staining, in a dose-dependent manner, in the *H. pylori*–infected GC mouse model (Fig. 6 K). Collectively, these results indicate that therapies with pharmacological targeting of IRF3 can effectively inhibit YAP-driven GC growth in xenograft and *H. pylori*–infected GC mouse models.

Pathological association between IRF3 and YAP in GC

Because cancer cells with elevated YAP expression were susceptible to treatment with Amlexanox, we asked whether YAP and IRF3 are pathologically associated with each other. We first analyzed the expression profiles of YAP and IRF3 in multiple cell lines. The mRNA levels of *IRF3* were positively correlated with those of *YAP* and *CTGF* in GC cells, as well as in cell lines of other cancers, including A549, HCT116, SW480, HeLa, Jurkat, and Raji cells (Fig. 7 A). Moreover, the protein levels of IRF3 were also correlated with those of YAP and its target gene *CTGF* in these cells (Fig. 7 B). Considering that activation of YAP requires its nuclear translocation and binding to TEAD4, and given that IRF3 acts as a "stabilizer" of the YAP–TEAD4 transactivation complex, we examined the amounts of YAP and IRF3 bound to TEAD4 in GC cells. Our coIP assay of endogenous proteins in HGC-27, MGC-803, MKN-1, BGC-823, and MKN-45 cells showed that the amount of YAP immunoprecipitated by a TEAD4-specific antibody was roughly correlated with that of IRF3 in the immunoprecipitates, suggesting a pathological association between IRF3 and YAP (Fig. 7 C).

Next, we examined the mRNA levels of *YAP* and *IRF3* in the *H. pylori*–infected GC mouse model. Consistent with a previous study (Jiao et al., 2014), we found that expressions of YAP and its target genes *CTGF* and *AXL* were significantly elevated in *H. pylori*–infected mice (Figs. 7 D and S5 H). In this progress of GC, IRF3 expression was also enhanced and correlated with YAP levels in these mice ($r = 0.612$, $P < 0.001$; Fig. 7 D). Subsequent analyses of clinical datasets available from the Gene Expression Omnibus (GEO) database (dataset accession no. GSE13911; D'Errico et al., 2009) revealed that both YAP and IRF3 were significantly up-regulated (at the mRNA level) in GC patients (Fig. S5, I and J). Moreover, the mRNA levels of *IRF3* were positively correlated with those of YAP/TEAD signature genes *AXL*, *BIRC5*, and *BCL2L1* in GC patients (Fig. S5 K).

To further verify the relevance of the observed correlation between IRF3 and YAP, we measured their mRNA levels in 90 human gastric tumor clinical specimens. Univariate analysis revealed that mRNA levels of *YAP* (50%) and *IRF3* (39%) were up-regulated in GC samples with increased expression of CTGF and AXL (Fig. 7 E). Moreover, up-regulation of *IRF3* was correlated with that of *YAP* (Table 1), as well as that of *CTGF* and *AXL* (Tables S10 and S11). In addition, we examined the phosphorylation level of IRF3 from clinical samples of two gastric tumor patients without antibiotic treatment. The protein levels of both nuclear IRF3/YAP and CTGF were elevated in GC tissues compared with those in paired normal tissues (Fig. 7 F). Notably, the phosphorylation levels of IRF3 were also elevated in GC samples, in keeping with hyperactivation of YAP.

To determine the potential association of IRF3 expression with clinical outcomes, we performed IHC staining of IRF3 and YAP on tissue microarrays containing 88 GC specimens that have a long-term clinical follow-up record. As shown in the representative images for cancer tissue and normal stomach membrane tissue from a single patient, the protein levels of IRF3 and YAP were both increased in cancer tissue, with a highly similar staining pattern in both the cytoplasm and the nucleus (Fig. 7 G). We also collected and preprocessed patients' data by extracting nine available clinical factors in two categories: the clinical background (age and gender) and the cancer stage information (tumor size, lymph node metastasis, distant metastasis, and tumor stage). IRF3 staining was significantly associated with tumor size ($P < 0.05$) but not significantly correlated with age, gender, lymph node metastasis, tumor metastasis, or tumor-node-metastatic stage (Fig. 7 H and Table 2). Similar observations were obtained for YAP (Fig. 7 H and Table S12). Subsequent Kaplan–Meier survival analysis showed that expression levels of IRF3 and YAP were both negatively correlated with 5-yr survival rate of GC patients (Figs. 7 I and S5 L). Moreover, GC patients with high levels of both IRF3 and YAP had shorter survival, whereas those with low levels of IRF3 and YAP had longer survival, again indicative of a pathological association between IRF3 and YAP (Fig. 7 I). Collectively, these results establish IRF3 as an independent prognostic marker for overall survival of GC patients (relative risk, 0.589; 95% confidence interval, ∼0.351 to ∼0.960; $P = 0.037$). Collectively, these results highlight the clinical relevance of IRF3 as a GC prognostic marker

Figure 6. **Pharmacological inhibition of IRF3 suppresses GC growth. (A)** Chemical structures of Amlexanox. **(B)** Cell proliferation of HGC27, BGC-823, and MKN45 cells after treatment with different doses of Amlexanox. **(C)** Colony formation of Amlexanox-treated cells. **(D)** Cell proliferation of YAP(S127)-overexpressing cells after treatment with Amlexanox. **(E)** Colony formation of YAP(S127A)-overexpressing cells after treatment with Amlexanox. **(F)** Cell viability of various cancer cells after treatment with different doses of Amlexanox. **(G)** Xenograft tumor growth of GC cell lines after treatment with Amlexanox. **(H)** Tumor volumes for the mice from G. **(I)** mRNA levels of YAP target genes in samples from G. **(J)** Tumor numbers in MNNG/HP-induced GC model after treatment with different doses of Amlexanox. **(K)** Ki67 staining of adenomas from J. Bar, 50 µm. At least two independent experiments were performed for all data. For curve figures and bar figures, data are presented as means ± SD. Unpaired Student's *t* tests were used for comparing two variables. One-way ANOVA was used for multiple variables comparison. *, $P < 0.05$; **, $P < 0.01$; ***, $P < 0.001$; *n.s.*, no significance in comparison with control group.

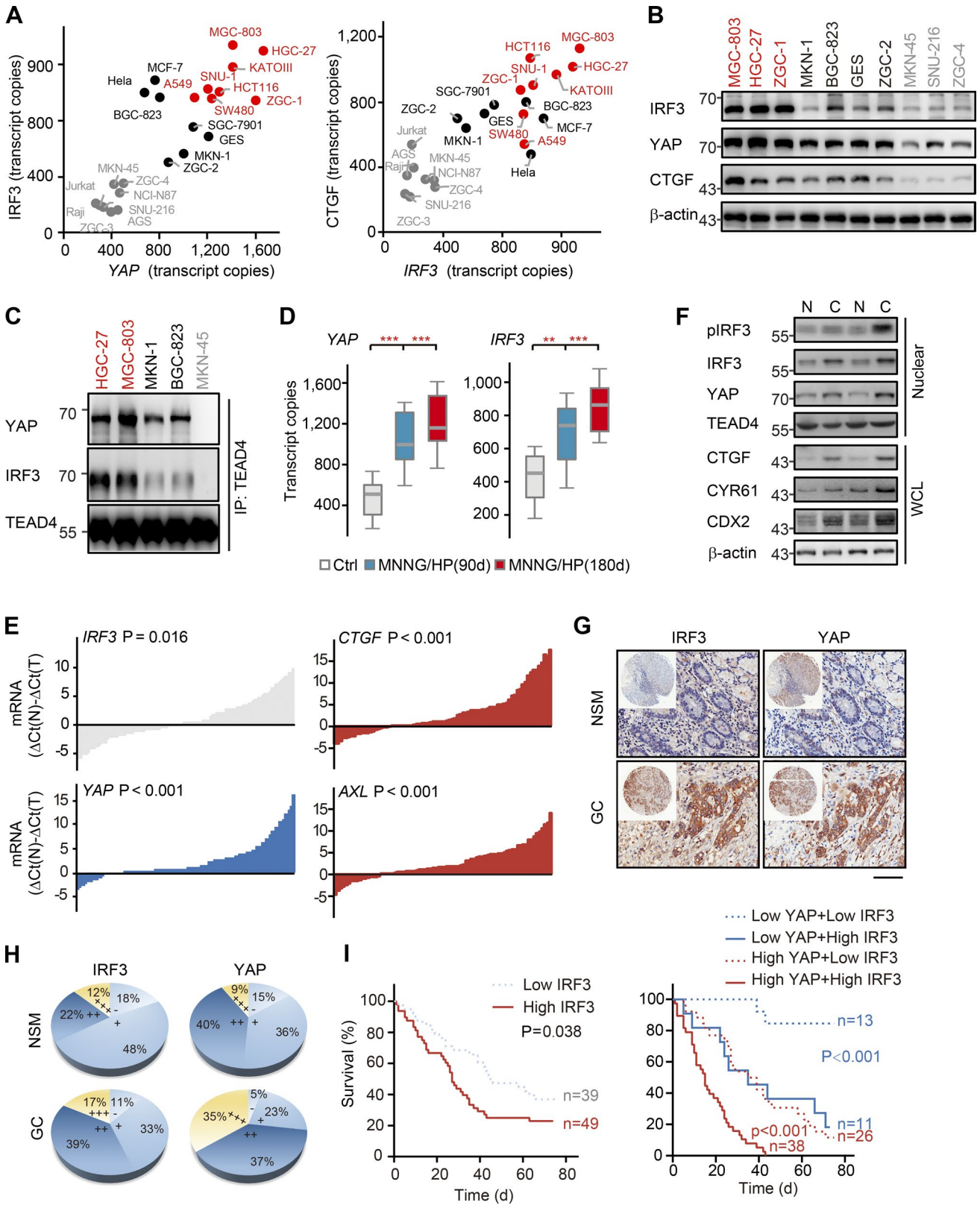

Figure 7. **Pathological association of IRF3 with YAP in GC. (A)** Scatter plot of positive correlation between *IRF3* and *YAP*/*CTGF* at the transcriptional level in different cancer cell lines. mRNA levels of *IRF3* were compared with those of *YAP* (left) and *CTGF* (right) by Spearman's correlation. **(B)** Western blotting of YAP, CTGF, and IRF3 in GC cell lines. **(C)** CoIP assay for detecting the association of YAP/IRF3 with TEAD4 in GC cells. **(D)** Box plots for mRNA

and demonstrate a close pathological association between IRF3 and YAP in GC pathogenesis.

DISCUSSION

The Hippo signaling pathway plays a key role in organ size control and tissue homeostasis, and dysregulation of this pathway has been linked to various cancers (Harvey and Tapon, 2007; Steinhardt et al., 2008; Pan, 2010; Zhao et al., 2010; Chan et al., 2011). Given the frequent hyperactivation of YAP in clinical samples of tumor patients, increasing efforts are being made to target YAP for therapeutic purposes (Cai et al., 2010; Liu-Chittenden et al., 2012; Koontz et al., 2013). However, the mechanism behind the nuclear translocation and activation of YAP remains poorly understood. In this study, we characterized IRF3, a transcription factor known to function centrally in innate antiviral immunity, as an agonist of YAP in GC.

Phosphorylation of YAP by the upstream kinase LATS1/2 leads to the retention of YAP in the cytoplasm. Once YAP enters the nucleus, it binds to its downstream transcription factor TEAD4, forming a transactivation complex to control target gene expression. Our current work refines this scenario by adding IRF3 as a positive regulator of YAP. IRF3 interacts with both YAP and TEAD4 in the nucleus to form a complex, which retains YAP in the nucleus and enhances the occupancy of YAP on target gene DNA. Despite the direct interaction between IRF3 and YAP/TEAD4, we speculate that TEAD4 binding to DNA may facilitate the recruitment of IRF3 into the complex. This could be the case even in the absence of classic IRF3-binding sites in the target genes. In this regard, note that DNA-facilitated transcription factor interaction/pairing has been recognized as a common theme for tailored specificity and cooperative regulation of gene expression (Jolma et al., 2015). Consistent with this notion, IRF3 is associated with YAP and TEAD4 genome-wide to coregulate the expression of a large group of target genes of the Hippo pathway. Furthermore, targeting IRF3 could effectively inhibit GC progression in a YAP-dependent manner. Moreover, IRF3 is highly correlated with YAP in clinical samples of GC patients, and elevated IRF3 levels are associated with poor prognosis.

The classically understood function of IRF3 is in cytosolic/viral nucleic acid sensing and antiviral immune responses (Akira et al., 2006; Wu and Chen, 2014). Our study revealed that a basal level of IRF3 is required for YAP activation, indicating an important physiological role of IRF3 as a YAP activator. Meanwhile, excessive IRF3 in cancer may exacerbate YAP-dependent tumor growth. In this regard, our findings are relevant to tumorigenesis involving viral infection. It is known that oncogenic viruses including HCV, HBV, Epstein-Barr virus, human papilloma virus, Kaposi's sarcoma herpes virus, and human T lymphotrophic virus 1 can cause oncogenesis of certain types of tumors (Akram et al., 2017). However, it remains unknown how infection-related immune signaling controls cancer development in general. Here, we observed that YAP activation was substantially induced in cells infected with viruses including HCV. In a pathological setting of virus infection, host immune response, especially IRF3-mediated antiviral signaling, may exacerbate tumor progression by directly promoting YAP activation. Thus, activation of IRF3 could be a risk factor for tumors with hyperactivation of YAP. Indeed, our results demonstrated that depletion of IRF3 substantially inhibited gastric tumor growth through down-regulation of YAP activity. In particular, pharmacological inhibition of IRF3 by Amlexanox inhibited the growth of tumor cells with YAP hyperactivation.

Interestingly, our study indicates a profound interdependency between tissue growth and immune defense, which has also been indicated by several recent studies published while this work was ongoing (Liu et al., 2016; Meng et al., 2016a; Wang et al., 2017; Zhang et al., 2017). For example, MST1 appears able to directly phosphorylate IRF3 and therefore inhibit its activation (Meng et al., 2016a). From the point of view of Hippo kinase, it appears that MST1 may block YAP activation not only through the LATS1/2 kinase, but also via inhibition of IRF3. However, we noticed that the conclusions of individual articles are not entirely consistent with each other on the surface, suggesting a complex interplay between the Hippo pathway and innate antiviral responses. For example, Wang et al. (2017) observed a negative role of YAP on IRF3 dimerization and found that YAP is targeted for lysosomal degradation by IKKε. Possible reasons for such a discrepancy include specific contexts such as cell type and cell confluence, certain experimental procedures such as duration of viral infection or treatment, and procedures for disease modeling in mice. In this regard, it is worth mentioning that we did not observe a significant change of the classic IRF3 target genes in the RNA-seq analysis of SeV-infected HGC-27 cells. A possible explanation is that the antiviral response occurs at an earlier stage before IRF3 regulation of YAP activity. Given the clinical relevance of IRF3 in GC and its

levels of *IRF3* and *YAP* in MNNG/HP samples. **(E)** mRNA levels of *IRF3*, *YAP*, *CTGF*, and *AXL* in GC. **(F)** Protein levels of IRF3, YAP, CTGF, CYR61, and CDX2 were elevated in GC samples. Molecular mass is indicated in kilodaltons. **(G)** Representative cores of YAP and IRF3 staining on tissue microarray. Bar, 100 µm. **(H)** Staining levels of YAP and IRF3 in normal and cancerous colon tissue indicating negative (–), weak (+), moderate (++), and strong (+++) expression levels. **(I)** Kaplan–Meier survival analysis of patients with YAP/IRF3 at high or low levels from tissue microarray. At least two independent experiments were performed for all data. For box figures, data are presented as means ± SD. Unpaired Student's *t* tests were used for comparing two variables. One-way ANOVA was used for multiple variables comparison. For correlation, the Spearman rank correlation was used for continuous variables. Survival curves were calculated according to the Kaplan–Meier method; survival analysis was performed using the log-rank test. **, $P < 0.01$; ***, $P < 0.001$ in comparison with control group.

Table 1. ***IRF3* mRNA levels are positively correlated with *YAP* mRNA levels in GC**

YAP mRNA	*IRF3* mRNA		Total
	Nonincreased	Increased	
Nonincreased	33	22	45
Increased	22	23	45
Total	55	35	90

P = 0.0299 by Fisher's exact test.

genome-wide association with YAP and TEAD4, this topic clearly warrants further investigation.

In summary, our work identifies IRF3 as an important YAP activator and provides a proof of concept that pharmacological targeting of IRF3 with small compound inhibitor can elicit a broad antitumor effect toward YAP-driven human cancers. These findings not only provide a molecular mechanism and functional importance of YAP regulation by IRF3, but also present a new therapeutic approach that may be combined with YAP inhibitors for targeted cancer therapies.

MATERIALS AND METHODS

Cell culture

HEK293FT, AGS, SNU-1, BGC-823, MGC-803, SGC-7901, HGC-27, NCI-N87, Jurkat, Raji, MCF-7, HeLa, and KATO III cells were obtained from the cell library of the Chinese Academy of Sciences (Shanghai, China). SNU-216 cells were purchased from ATCC. MKN-1, MKN-45, and GES cells were from the RIKEN BioResource Center.

HEK293FT, HeLa, MCF-7, SW480, and HCT116 cells were grown in DMEM (Invitrogen). All other cells were cultured in RPMI 1640 (Invitrogen). All cell lines were maintained in culture supplemented with 10% heat-inactivated FCS, 100 µg/ml penicillin, and 100 µg/ml streptomycin at 37°C with 5% CO_2 in a humidified incubator (Thermo). The cells were passaged for ≤3 mo from the frozen early passage stocks that had been received from the indicated sources. All cells were maintained in appropriate media; 10% heat-inactivated FCS, 100 µg/ml penicillin, and 100 µg/ml streptomycin were added to all media, and cells were cultured at 37°C with 5% CO_2 in a humidified incubator. During the study, all cell cultures were periodically tested for mycoplasma using MycoAlert Mycoplasma Detection kits (Lonza).

Reagents and antibodies

Poly(I:C) (P1530), poly(dA:dT) (P0883), Amlexanox (SML0517), 5-FU (F6627), and antibodies specific for Flag (M3165), α-tubulin (T6199), and β-actin (A2228) were from Sigma-Aldrich. Antibodies specific for pIRF3-396 (29047), IRF3 (11904, Western blot [WB]/immunofluorescence [IF]), MST1 (3682), pMOB1-T35 (8699), MOB1 (13730), LATS1 (3477), SAV1 (13301), pYAP-S127 (13008), pYAP-397 (13619), YAP (14074, ChIP), MAVS (3993), STING (13647), and HA (3724, WB/IF/ChIP) were from Cell Signaling Technology; those for IRF3 (sc-9082, IHC/ChIP), YAP (sc-271134, WB), and TEAD4 (sc-101184, ChIP) were from Santa Cruz Biotechnology; and those for Ki67 (ab15580), TEAD4 (ab58310), and YAP (ab39361, IP/IF/IHC) were from Abcam. Phos-tag–conjugated acrylamide was purchased from Wako Chemicals.

Table 2. **Clinical significance of IRF3 expression in GC**

Groups	IRF3 expression				*n*	Positive	P-value (Fisher's test)
	–	+	+ +	+ + +			
						%	
Gender							0.5761
Male	8	23	25	9	65	87.7	
Female	2	6	9	6	23	91.3	
Age							0.5336
<60	4	8	10	7	29	86.2	
≥60	6	21	24	8	59	89.8	
Tumor size							0.0478[a]
pT1 + pT2	4	2	3	3	12	66.7	
pT3 + pT4	6	27	31	12	76	92.1	
Lymph node metastasis							0.0711
N0 + N1	7	14	9	6	36	80.6	
N2 + N3	3	15	25	9	52	94.2	
Distant metastasis							0.5013
M0	10	29	32	14	85	88.2	
M1	0	0	2	1	3	100.0	
Tumor stage							0.1097
I + II	6	15	9	7	37	83.8	
III + IV	4	14	25	8	51	92.1	
Total	10	29	34	15	88		

[a]Statistically significant; P < 0.05.

Plasmids

Mammalian expression vectors for YAP, RIG-I (CA), MAVS, TBK1, and IRF3 were described previously (Jiao et al., 2014; Hao et al., 2015). IRF3(5D) (S396D/S398D/S402D/S405D/T404D) plasmid was kindly provided by P. Xu from Zhejiang University (Hangzhou, China). All lentiviral plasmids were constructed in a modified pLKO.1 vector. Two pairs of shRNA oligos of IRF3 were designed and synthesized. For oligo-1 (from the coding sequence of IRF3): forward oligo, 5′-CCGGGGAGGCAGTACTTCTGATACTCGAGTATCAGAAGTACTGCCTCCTTTTTG-3′; reverse oligo, 5′-AATTCAAAAAGGAGGCAGTACTTCTGATACTCGAGTATCAGAAGTACTGCCTCC-3′. For oligo-2 (from the 5′-UTR sequence of IRF3), forward oligo, 5′-CCGGGGGTCTGTTACCCAAAGAACTCGAGTTCTTTGGGTAACAGACCCTTTTTG-3′; reverse oligo, 5′-AATTCAAAAAGGGTCTGTTACCCAAAGAACTCGAGTTCTTTGGGTAACAGACCC-3′. A scramble DNA duplex was also designed as a control.

siRNAs

Duplexes for the siRNA targeting of YAP, MAVS, STING, IRF3, and n.c. were synthesized by Genepharma. The siRNA sequences are as follows. For human siYAP-1: forward oligo,

5′-CUGCCACCAAGCUAGAUAATT-3′, and reverse oligo, 5′-UUAUCUAGCUUGGUGGCAGTT-3′; for human siYAP-2: forward oligo, 5′-GGUGAUACUAUCAACCAA ATT-3′; reverse oligo, 5′-UUUGGUUGAUAGUAUCAC CTT-3′; for human siMAVS-1: forward oligo, 5′-CAUCCA AAUUGCCCAUCAATT-3′; reverse oligo, 5′-UUGAUG GGCAAUUUGGAUGTT-3′; for human siMAVS-2: forward oligo, 5′-CACAGGGUCAGUUGUAUCUTT-3′; reverse oligo, 5′-AGAUACAACUGACCCUGUGTT-3′; for human siSTING-1: forward oligo, 5′-GCCCUUCACUUG GAUGCUUTT-3′; reverse oligo, 5′-AAGCAUCCAAGU GAAGGGCTT-3′; for human siSTING-2: forward oligo, 5′-CCCGGAUUCGAACUUACAATT-3′; reverse oligo, 5′-UUGUAAGUUCGAAUCCGGGTT-3′; for human siIRF3-1: forward oligo, 5′-CAGGAGGAUUUCGGAAUC UTT-3′; reverse oligo, 5′-AGAUUCCGAAAUCCUCCU GTT-3′; for human siIRF3-2: forward oligo, 5′-GGAGGC AGUACUUCUGAUATT-3′; reverse oligo, 5′-UAUCAG AAGUACUGCCUCCTT-3′; and for n.c.: forward oligo, 5′-UUCUCCGAACGUGUCACGUTT-3′; reverse oligo, 5′-ACGUGACACGUUCGGAGAATT-3′.

Transfection, viral infection, and luciferase assay

Approximately 0.5–1 μg/ml poly(I:C) and ∼0.5–1 μg/ml poly(dA:dT) were transfected using Lipofectamine 2000 from Invitrogen according to the manufacturer's instructions. Where indicated, cells were infected with SeV (MOI 1),VSV (MOI 0.1), or HCV (MOI 0.1) in serum-free medium for the indicated times. 1 h later, cells were rinsed and cultured in fresh medium. To select stable transfectants, the cells were transfected and incubated overnight, and then switched to a medium containing 600 μg/ml G418 for further incubation. The medium that contained G418 was changed every 2–3 d. After 2 wk, isolated colonies began to appear. In 3 wk, a pool of G418-resistant cells was selected for further studies. The luciferase activities were determined using the Dual-luciferase Assay System (Promega).

Real-time PCR

Real-time PCR was performed on a Two-Step Real-Time PCR System (Applied Biosystems) using the comparative Ct quantization method. Real-time PCR Master Mix (Toyobo) was used to detect and quantify the expression level of the target gene. GAPDH was used as an internal control. The primers used were as follows: *hIRF3*: forward, 5′-AGAGGC TCGTGATGGTCAAG-3′, and reverse, 5′-AGGTCCACA GTATTCTCCAGG-3′ (R); *hIFNB*: forward, 5′-ATGACC AACAAGTGTCTCCTCC-3′, and reverse, 5′-GGAATC CAAGCAAGTTGTAGCTC-3′; *hIFNB* (ChIP): forward, 5′-GCCAGGAGCTTGAATAAAATG-3′, and reverse, 5′-CTGTCAAAGGCTGCAGTGAG-3′; *hYAP*: forward, 5′-GCATGATCTGCCCTAAGGC-3′, and reverse, 5′-TGA CCGCCGAGTACACCAT-3′; *hCTGF*: forward, 5′-AAA AGTGCATCCGTACTCCCA-3′, and reverse, 5′-CCG TCGGTACATACTCCACAG-3′; *hCTGF* (ChIP): forward, 5′-CTTCTTGGTGTTGTGCTGGA-3′, and reverse, 5′-GATTGATCCTGACCCCTTGA-3′; *hCYR61*: forward, 5′-GGTCAAAGTTACCGGGCAGT-3′, and reverse, 5′-GGAGGCATCGAATCCCAGC-3′; *hGAPDH*: forward, 5′-GGCATCCTGGGCTACACTGA-3′, and reverse, 5′-GAG TGGGTGTCGCTGTTGAA-3′; *mIRF3*: forward, 5′-GAG CGCCGAACGAGGTTCAG-3′, and reverse, 5′-CTTCCA GGTTGACACGTCCG-3′; *mYAP*: forward, 5′-TGAGAT CCCTGATGATGTACCAC-3′, and reverse, 5′-TGTTGT TGTCTGATCGTTGTGAT-3′; *mCTGF*: forward, 5′-GGA CACCTAAAATCGCCAAGC-3′, and reverse, 5′-ACT TAGCCCTGTATGTCTTCACA-3′; *mCYR61*: forward, 5′-TAAGGTCTGCGCTAAACAACTC-3′, and reverse, 5′-CAGATCCCTTTCAGAGCGGT-3′; and *mGAPDH*: forward, 5′-AATGGATTTGGACGCATTGGT-3′, and reverse, 5′-TTTGCACTGGTACGTGTTGAT-3′.

RNA sequencing

HGC-27 cells were reverse transfected with siRNAs for 48 h in 6-well plates. RNA was extracted from two biological replicates. RNA quality was assessed on a 2100 expert Bioanalyzer (Agilent) and sent for library preparation and sequencing on the Illumina Hiseq2000 platform by BGI Genomics (Wuhan, China).

Cell proliferation assay

An ATP-based cell viability assay was used for detecting cell proliferation. ATP content was measured in accordance with the instructions for a CellTiter-Glo luminescent cell viability assay kit (Promega). In brief, 100 μl of assay reagent was added to the wells and mixed for 2 min at room temperature. After 10 min, intracellular ATP content was measured using a multilabel luminescence counter (Envision; Perkin Elmer). Cell viability was calculated using the following equation: % cell viability = [value (test) − value (blank)] × [value (control) − value (blank)]$^{-1}$ × 100.

Soft agar colony formation

A total of 10^4 cells were seeded on soft agar in 6-well plates, and colonies with a diameter of >1 mm were counted 14 d after seeding.

Xenograft tumor formation

Healthy BALB/cA-nu/nu mice (6 wk) were obtained from the Shanghai Experimental Animal Center and maintained in pathogen-free conditions. During the tumor formation assay, cancer cell lines were injected into the flank of the mice (HGC-27, 10^6; BGC-823 or HGC-27, 10^6; MKN-45, 2×10^6). Once tumors were detected, mice were fed once daily with Amlexanox in corn oil (0.1-ml volume) via an intragastric gavage using a ball-tipped needle. Mice were randomized to receive either 5 or 50 mg/kg per day of Amlexanox. In addition, mice were treated intravenously with 50 mg/kg 5-FU as a positive control. Mice were sacrificed after 4 wk, and tumor volumes were then measured. These animal

experiments followed a double-blind study design. All animals were randomly assigned to treatment groups in all experiments, and experiments were conducted in accordance with the guidelines of the Institutional Animal Care and Use Committee of the Institute of Biochemistry and Cell Biology. The approval ID for the use of animals was 081, issued by the Animal Core Facility of SIBCB.

Generation of IRF3 KO mice using CRISPR-Cas9 genome editing

Cas9 knock-in mice (C57BL/6J background) were provided by D. Zhou from Xiameng University (Fujian Sheng, China). IRF3 sgRNA sequences were as follows: sgIrf3-1, 5′-CGTGGGAGTGGCCTAGGCGC-3′; sgIrf3-2, 5′-GGCGCGGGACTTCGTACATC-3′; sgIrf3-3, 5′-ACGGAGCCGTGTTCGACCTC-3′; sgIrf3-4, 5′-ACGTCCGGCTTATCCTTCCC-3′; sgIrf3-5, 5′-CTAACCGCAACACTTCTTTC-3′; and sgIrf3-6, 5′-AACCTACCGAAGTTATTTGA-3′.

A control sgRNA sequence was designed to target the *lacZ* gene from *Escherichia coli*. The synthesis and characterization of pH-responsive diblock copolymers and the resulting nanoparticles followed previously described methods. In brief, reversible addition fragmentation chain transfer polymerization was used to polymerize dimethylaminoethyl methacrylate (DMAEMA) blocks. The polymerization was conducted in a nitrogen atmosphere in *N*,*N*-dimethylformamide (DMF) at 30°C for 12 h. To add the second block of the diblock copolymer, pDMAEMA macroCTA was isolated and added to DMAEMA, propyl acrylic acid, and butyl methacrylate in DMF at 1:1:2 molar ratios. Diblock copolymers were solubilized in highly concentrated stock solutions (~1 g/ml) in ethanol and diluted to 2 mg/ml in PBS. This solution was then used to form complexes with sgRNA and injected into mice (i.v.). The size of complexes (or polymer alone) was 50–60 nm. The mice were randomly divided into two groups, which received either control sgRNA nanoparticles or sgIrf3 nanoparticles.

MNNG-induced GC mice model

IRF3$^{-/-}$ mice and their WT littermates (4 wk) were housed in an air-conditioned biohazard room designed for infectious animals, with a 12-h light/dark cycle. The mice were inoculated with *H. pylori* SS1 or YAP/YAP (5A) lentivirus intragastrically. Normal mice (n = 20) were given same amount of normal saline and were housed in isolators to prevent risk of infection.

Immunofluorescence

293FT or HGC-27 cells were plated on coverslips in 33-mm dishes after different treatments. Coverslips with the cells were washed once with PBS and fixed in 4% formaldehyde in PBS for 15 min. After permeabilization with Triton X-100 (0.25%) in PBS for 15 min, cells were blocked with PBS containing BSA (5%) for 1 h and then incubated with primary antibodies for 1 h. After three separate washes, cells were incubated with a secondary antibody for another hour and then stained with DAPI for two minutes. The coverslips were washed extensively and fixed on slides. Images were captured using SIM equipped with Nikon Apo TIRF 100× NA 1.49 oil immersion objective and four lasers (405, 488, 561, and 640 nm). All SIM images were cropped and processed by NIS-Elements Viewer 4.50.

Immunoprecipitation and immunoblotting

For immunoprecipitation experiments, whole-cell extracts were prepared with or without 10 μg/ml DNase I after transfection or stimulation and were incubated overnight with primary antibodies (0.6 μg/ml protein) together with protein A/G beads (Santa Cruz Biotechnologies). Beads were then washed three times with lysis buffer, and immunoprecipitates were eluted with SDS loading buffer and resolved in SDS-PAGE gels. The proteins were transferred to a PVDF membrane (Bio-Rad) and further incubated with the secondary antibodies. The phos-tag gels containing phos-tag were prepared according to the manufacturer's instructions.

Pull-down assay

MBP-fused proteins immobilized on Amylose Resin (New England Biolabs) were incubated with different prey proteins in the binding buffer containing 100 mM Tris, pH 8.0, 150 mM NaCl, 0.1% vol/vol Triton X-100, and 10 mM β-mercaptoethanol at 4°C. After 2 h, the beads were washed three times with binding buffer and eluted with the same buffer plus 10 mM maltose monohydrate (Sigma-Aldrich). The immobilized proteins were visualized with either Coomassie blue staining or Western blotting.

ChIP and ChIP-Seq

Cells were suspended in 5× volume of cell lysis buffer (10 mM Hepes-KOH, pH 7.8, 10 mM KCl, 0.1 mM EDTA, and 0.1% NP-40) and incubated for 5 min on ice. The suspension was centrifuged at 700 *g* for 3 min and then resuspended in a 3× volume of cell lysis buffer using a 21-G syringe. The suspension was centrifuged at 700 *g* for 3 min, and the sedimented nuclei were resuspended in 9.5 ml PBS. The nuclei were initially fixed by adding 0.5 ml of 20 mM DSP and rotated for 30 min at 25°C. The suspension was centrifuged at 190 *g* for 3 min, and nuclei were fixed with 1% formaldehyde for 10 min at 25°C. The reaction was stopped by adding 0.5 ml of 2.5 M glycine and rotating samples for 5 min. The suspension was centrifuged at 700 *g* for 3 min and then resuspended in 0.3 ml nucleic lysis buffer (10 mM Tris-HCl, pH 7.5, 200 mM NaCl, 10 mM EDTA, and 1% SDS) containing proteinase inhibitors. Lysates were sonicated to yield ~300–1,000-bp DNA fragments. After elimination of cell debris by centrifugation, the sample was diluted with 1.8 ml ChIP dilution buffer and precleared with 10 μl protein A–Sepharose (50% slurry) for 30 min at 4°C with agitation. The sample (0.1 ml) was saved to assess input DNA. Approximately 2–5 μg of the antibodies, including HA antibody (3724), YAP antibody

(14074), IRF3 antibody (sc-9082), and TEAD4 antibody (sc-101184), was incubated with the sheared cross-linked chromatin to immunoprecipitate the indicated complexes. Input and immunoprecipitated DNA were subjected to Sybergreen quantitative PCR cycles with primers overlapping the gene body and the upstream and downstream regulatory regions of target genes. For ChIP-seq, ∼200 µg chromatin was incubated with 10 µg antibody overnight at 4°C. Antibody–antigen complexes were recovered with ProteinA-Dynabeads (Invitrogen) for 2 h at 4°C. ChIP'd DNA from three immunoprecipitations was pooled to generate libraries with the Ovation Ultra Low Library Prep kit (NuGEN) according to the manufacturer's instructions. Sequencing was performed on an Illumina HiSeq 2500 platform.

Peak calling and data analysis

Raw reads were aligned using Bowtie (version 1.2.1.1; Langmead et al., 2009) to build version hg38 of the human genome retaining only uniquely mapped reads. Redundant reads were removed using SAMtools. The irreproducible discovery rate (IDR) framework was used to assess the consistency of replicate experiments and to obtain a high-confidence single set of peak calls for each transcription factor as described in the ChIP-seq guidelines of the ENCODE consortium. MACS2 v.2.0.10 was used to call peaks in individual replicates using IgG ChIP-seq as the control sample, and an IDR threshold of 0.01 was applied for all datasets to identify an optimal number of peaks (Zhang et al., 2008b). Normalized read density (reads per million) was calculated from pooled replicates using the MACS2 callpeak function and displayed using the Integrative Genomics Viewer (IGV). Heat maps were generated using a custom R script that considers a 2-kb window centered on peak summits and calculates the normalized read density with a resolution of 50 bp. The genomic location of the peaks and their distance to the TSS of annotated genes were calculated using the annotatePeakInBatch function of the ChIPpeakanno R package and GENCODE annotation (Harrow et al., 2012). Only genes classified as protein coding and with status equal to known were considered.

Collection of human GC specimens

Tissue specimens were collected for quantitative RT-PCR and Western blot analysis from 90 patients with GC who underwent gastrectomy between 2007 and 2008. All cases of GC and adjacent nontumor tissues were diagnosed clinically and pathologically. Data on pathological features and prognoses of the patients were collected and analyzed retrospectively. The disease stage of each patient was classified or reclassified according to the 2009 American Joint Committee on Cancer staging system. A total of 88 patients were followed up until August 2013; two of them were lost during the follow-up period. Other research specimens included fast-frozen tissue for RNA isolation and paraffin-embedded tissue for continued histological observation. All samples collected and used were derived from patients who signed an informed consent that was approved by the Ethics Committee of Taizhou Hospital of Zhejiang province. All patients receiving treatment in this study were treated as part of a clinical protocol.

Tissue microarray and IHC staining

GC and normal tissue microarray sections were prepared by Shanghai Outdo Biotech Co. Ltd. (Shanghai, China). This tissue array contains tissues from 88 paired fresh gastric carcinoma and normal tissue samples, and was used to examine the expression profiles of YAP and IRF3 by IHC. For IHC, TMA sections were incubated with anti-Ki67 antibody (1:100 dilution), anti-YAP antibody (1:100 dilution), or anti-IRF3 antibody (1:50 dilution). IHC stains were scored by two independent pathologists who were blinded to the clinical characteristics of the patients. The scoring system was based on the intensity and extent of staining: staining intensity was classified as 0 (negative), 1 (weak), 2 (moderate), or 3 (strong); staining extent was dependent on the percentage of positive cells (examined in 200 cells) and was classified into 0 (<5%), 1 (5–25%), 2 (26–50%), 3 (51–75%), or 4 (>75%). According to the staining intensity and staining extent scores, the IHC result was classified as 0–1, negative (–); 2–4, weakly positive (+); 5–8, moderately positive (++), and 9–12, strongly positive (+++).

Statistical analysis

Both cellular and animal studies tended to be underpowered. Estimation of sample size for planned comparisons of two independent means using a two-tailed test were undertaken using an online calculator and in the SAS statistical software package (9.1.3). Data are expressed as mean ± SD for continuous variables and as frequencies and proportions for categorical variables. Continuous data were compared using Student's *t* tests (comparing two variables) or one-way ANOVA analysis (comparing multiple variables). For correlation, the Spearman rank correlation was used for continuous variables. Survival curves were calculated according to the Kaplan–Meier method; survival analysis was performed using the log-rank test. $P < 0.05$ was considered to indicate a significant difference. To detect significant regions bound with each factor from ChIP-seq data during MACS2, the threshold of $q < 0.0001$ was used. Two to three biological replicates were used throughout the study.

Accession numbers

The GEO accession numbers for the high-throughput sequencing reported in this paper are GSE109028 and GSE107096.

Online supplemental material

Fig. S1 shows that nucleic acids mimicking viral infection induce YAP activation through IRF3 signaling. Fig. S2 shows the complex of IRF3-YAP-TEAD4. Fig. S3 depicts co-occupancy of IRF3 and YAP/TEAD on the promoter of the Hippo targeted genes. Fig. S4 shows that knockdown of IRF3 inhibits YAP-dependent cell proliferation. Fig. S5 reveals the

positive association between YAP and IRF3. Table S1 presents an RNA-seq that identified 1,458 differentially regulated genes between PBS-treated and SeV-treated cells. Tables S2, S3, and S4 are lists for YAP/TAZ/TEAD direct target genes from three independent studies. Table S5 shows a ChIP-seq that reveals the co-occupancy peaks of YAP/TEAD4/IRF3 at genomic levels. Table S6 is a list of YAP/TEAD4/IRF3 direct target genes. Table S7 presents an RNA-seq that identified 1,608 differentially regulated genes in HGC-27 cells after transfection with siIRF3. Table S8 and S9 are lists of siIRF3- and siYAP-regulated genes in the core enrichment of the YAP target gene set. Tables S10 and S11 reveal a positive association between IRF3 and CTGF/AXL in GC. Table S12 lists the clinical significance of YAP expression in GC.

ACKNOWLEDGMENTS

We appreciate the generous support by Prof. Naihe Jing and Prof. Jinqiu Zhou and helpful discussions with Dr. Dangsheng Li at Shanghai Institute of Biochemistry and Cell Biology. We are very grateful to Prof. Pinglong Xu at Zhejiang University and Prof. Dawang Zhou at Xiamen University for their cooperation. We thank the National Center for Protein Science Shanghai for the confocal laser-scanning microscope, and we are grateful to Yan Wang for her great technical assistance.

This work was supported by the National Key R&D Program of China (grant 2017YFA0504504), the National Natural Science Foundation of China (grants 91442125, 31470736, 31470868, 91542125, 81773212, and 81725014), the Strategic Priority Research Program (grants XDB19020202 and XDA12020342), the Science and Technology Commission of Shanghai Municipality (grants 17YF1422200 and 17ZR1435400), and the Youth Innovation Promotion Association of the Chinese Academy of Sciences. We gratefully acknowledge the support of the SA-SIBS Scholarship Program.

The authors have filed a patent (201711022197.9) about therapeutic targeting of IRF3-YAP. The authors declare no further conflicts of interests.

Author contributions: S. Jiao and J. Guan performed most cellular experiments and in vivo analyses. M. Chen, W. Wang and Y. Wang made constructs for YAP and IRF3 and carried out biochemical analysis. C. Li performed some of the immunofluresscent assays. Y. Cheng helped in data analysis and discussion. S. Jiao and Z. Zhou designed the experiments, analyzed the data, and wrote the manuscript. Z. Zhou supervised the project.

Submitted: 21 June 2017

Revised: 7 November 2017

Accepted: 12 December 2017

REFERENCES

Akira, S., S. Uematsu, and O. Takeuchi. 2006. Pathogen recognition and innate immunity. *Cell.* 124:783–801. https://doi.org/10.1016/j.cell.2006.02.015

Akram, N., M. Imran, M. Noreen, F. Ahmed, M. Atif, Z. Fatima, and A. Bilal Waqar. 2017. Oncogenic role of tumor viruses in humans. *Viral Immunol.* 30:20–27. https://doi.org/10.1089/vim.2016.0109

Bahrami, A., F. Amerizadeh, S. ShahidSales, M. Khazaei, M. Ghayour-Mobarhan, H.R. Sadeghnia, M. Maftouh, S.M. Hassanian, and A. Avan. 2017. Therapeutic potential of targeting Wnt/β-catenin pathway in treatment of colorectal cancer: Rational and progress. *J. Cell. Biochem.* 118:1979–1983. https://doi.org/10.1002/jcb.25903

Cai, J., N. Zhang, Y. Zheng, R.F. de Wilde, A. Maitra, and D. Pan. 2010. The Hippo signaling pathway restricts the oncogenic potential of an intestinal regeneration program. *Genes Dev.* 24:2383–2388. https://doi.org/10.1101/gad.1978810

Chan, S.W., C.J. Lim, L. Chen, Y.F. Chong, C. Huang, H. Song, and W. Hong. 2011. The Hippo pathway in biological control and cancer development. *J. Cell. Physiol.* 226:928–939. https://doi.org/10.1002/jcp.22435

D'Errico, M., E. de Rinaldis, M.F. Blasi, V. Viti, M. Falchetti, A. Calcagnile, F. Sera, C. Saieva, L. Ottini, D. Palli, et al. 2009. Genome-wide expression profile of sporadic gastric cancers with microsatellite instability. *Eur. J. Cancer.* 45:461–469. https://doi.org/10.1016/j.ejca.2008.10.032

Deitrick, J., and W.M. Pruitt. 2016. Wnt/β Catenin-Mediated Signaling Commonly Altered in Colorectal Cancer. *Prog. Mol. Biol. Transl. Sci.* 144:49–68. https://doi.org/10.1016/bs.pmbts.2016.09.010

Fitzgerald, K.A., S.M. McWhirter, K.L. Faia, D.C. Rowe, E. Latz, D.T. Golenbock, A.J. Coyle, S.M. Liao, and T. Maniatis. 2003. IKKepsilon and TBK1 are essential components of the IRF3 signaling pathway. *Nat. Immunol.* 4:491–496. https://doi.org/10.1038/ni921

Goulev, Y., J.D. Fauny, B. Gonzalez-Marti, D. Flagiello, J. Silber, and A. Zider. 2008. SCALLOPED interacts with YORKIE, the nuclear effector of the hippo tumor-suppressor pathway in Drosophila. *Curr. Biol.* 18:435–441. https://doi.org/10.1016/j.cub.2008.02.034

Halder, G., and R.L. Johnson. 2011. Hippo signaling: growth control and beyond. *Development.* 138:9–22. https://doi.org/10.1242/dev.045500

Hao, Q., S. Jiao, Z. Shi, C. Li, X. Meng, Z. Zhang, Y. Wang, X. Song, W. Wang, R. Zhang, et al. 2015. A non-canonical role of the p97 complex in RIG-I antiviral signaling. *EMBO J.* 34:2903–2920. https://doi.org/10.15252/embj.201591888

Harrow, J., A. Frankish, J.M. Gonzalez, E. Tapanari, M. Diekhans, F. Kokocinski, B.L. Aken, D. Barrell, A. Zadissa, S. Searle, et al.2012. GENCODE: the reference human genome annotation for The ENCODE Project. Genome Res.22:1760–1764.

Harvey, K., and N. Tapon. 2007. The Salvador-Warts-Hippo pathway—An emerging tumour-suppressor network. *Nat. Rev. Cancer.* 7:182–191. https://doi.org/10.1038/nrc2070

Hong, A.W., Z. Meng, and K.L. Guan. 2016. The Hippo pathway in intestinal regeneration and disease. *Nat. Rev. Gastroenterol. Hepatol.* 13:324–337. https://doi.org/10.1038/nrgastro.2016.59

Huang, J., S. Wu, J. Barrera, K. Matthews, and D. Pan. 2005. The Hippo signaling pathway coordinately regulates cell proliferation and apoptosis by inactivating Yorkie, the Drosophila Homolog of YAP. *Cell.* 122:421–434. https://doi.org/10.1016/j.cell.2005.06.007

Jiao, S., H. Wang, Z. Shi, A. Dong, W. Zhang, X. Song, F. He, Y. Wang, Z. Zhang, W. Wang, et al. 2014. A peptide mimicking VGLL4 function acts as a YAP antagonist therapy against gastric cancer. *Cancer Cell.* 25:166–180. https://doi.org/10.1016/j.ccr.2014.01.010

Jiao, S., C. Li, Q. Hao, H. Miao, L. Zhang, L. Li, and Z. Zhou. 2017. VGLL4 targets a TCF4-TEAD4 complex to coregulate Wnt and Hippo signalling in colorectal cancer. *Nat. Commun.* 8:14058. https://doi.org/10.1038/ncomms14058

Jolma, A., Y. Yin, K.R. Nitta, K. Dave, A. Popov, M. Taipale, M. Enge, T. Kivioja, E. Morgunova, and J. Taipale. 2015. DNA-dependent formation of transcription factor pairs alters their binding specificity. *Nature.* 527:384–388. https://doi.org/10.1038/nature15518

Koontz, L.M., Y. Liu-Chittenden, F. Yin, Y. Zheng, J. Yu, B. Huang, Q. Chen, S. Wu, and D. Pan. 2013. The Hippo effector Yorkie controls normal tissue growth by antagonizing scalloped-mediated default repression. *Dev. Cell.* 25:388–401. https://doi.org/10.1016/j.devcel.2013.04.021

Langmead, B., C. Trapnell, M. Pop, and S.L. Salzberg. 2009. Ultrafast and memory-efficient alignment of short DNA sequences to the human genome. Genome Biol.10:R25.

Lin, R., C. Heylbroeck, P.M. Pitha, and J. Hiscott. 1998. Virus-dependent phosphorylation of the IRF-3 transcription factor regulates nuclear translocation, transactivation potential, and proteasome-mediated

degradation. *Mol. Cell. Biol.* 18:2986–2996. https://doi.org/10.1128/MCB.18.5.2986

Liu, B., Y. Zheng, F. Yin, J. Yu, N. Silverman, and D. Pan. 2016. Toll receptor-mediated hippo signaling controls innate immunity in Drosophila. *Cell.* 164:406–419. https://doi.org/10.1016/j.cell.2015.12.029

Liu, J., X. Zeng, Q. Chen, Y. Cai, F. Chen, Y. Wang, H. Zhou, M. Lin, J. Shi, Z. Wang, and Y. Zhang. 2006. An evaluation on the efficacy and safety of amlexanox oral adhesive tablets in the treatment of recurrent minor aphthous ulceration in a Chinese cohort: a randomized, double-blind, vehicle-controlled, unparallel multicenter clinical trial. *Oral Surg. Oral Med. Oral Pathol. Oral Radiol. Endod.* 102:475–481. https://doi.org/10.1016/j.tripleo.2005.12.014

Liu-Chittenden, Y., B. Huang, J.S. Shim, Q. Chen, S.J. Lee, R.A. Anders, J.O. Liu, and D. Pan. 2012. Genetic and pharmacological disruption of the TEAD-YAP complex suppresses the oncogenic activity of YAP. *Genes Dev.* 26:1300–1305. https://doi.org/10.1101/gad.192856.112

Meng, F., R. Zhou, S. Wu, Q. Zhang, Q. Jin, Y. Zhou, S.W. Plouffe, S. Liu, H. Song, Z. Xia, et al. 2016a. Mst1 shuts off cytosolic antiviral defense through IRF3 phosphorylation. *Genes Dev.* 30:1086–1100. https://doi.org/10.1101/gad.277533.116

Meng, W., Y. Dong, J. Liu, Z. Wang, X. Zhong, R. Chen, H. Zhou, M. Lin, L. Jiang, F. Gao, et al. 2009. A clinical evaluation of amlexanox oral adhesive pellicles in the treatment of recurrent aphthous stomatitis and comparison with amlexanox oral tablets: A randomized, placebo controlled, blinded, multicenter clinical trial. *Trials.* 10:30. https://doi.org/10.1186/1745-6215-10-30

Meng, Z., T. Moroishi, and K.L. Guan. 2016b. Mechanisms of Hippo pathway regulation. *Genes Dev.* 30:1–17. https://doi.org/10.1101/gad.274027.115

Murray, B., N. McGuinness, P. Biagioni, P. Hyland, and P.J. Lamey. 2005. A comparative study of the efficacy of Aphtheal in the management of recurrent minor aphthous ulceration. *J. Oral Pathol. Med.* 34:413–419. https://doi.org/10.1111/j.1600-0714.2005.00334.x

O'Neill, L.A., and A.G. Bowie. 2010. Sensing and signaling in antiviral innate immunity. *Curr. Biol.* 20:R328–R333. https://doi.org/10.1016/j.cub.2010.01.044

Pan, D. 2010. The hippo signaling pathway in development and cancer. *Dev. Cell.* 19:491–505. https://doi.org/10.1016/j.devcel.2010.09.011

Servant, M.J., B. ten Oever, C. LePage, L. Conti, S. Gessani, I. Julkunen, R. Lin, and J. Hiscott. 2001. Identification of distinct signaling pathways leading to the phosphorylation of interferon regulatory factor 3. *J. Biol. Chem.* 276:355–363. https://doi.org/10.1074/jbc.M007790200

Sharma, S., B.R. tenOever, N. Grandvaux, G.P. Zhou, R. Lin, and J. Hiscott. 2003. Triggering the interferon antiviral response through an IKK-related pathway. *Science.* 300:1148–1151. https://doi.org/10.1126/science.1081315

Shi, Z., F. He, M. Chen, L. Hua, W. Wang, S. Jiao, and Z. Zhou. 2017. DNA-binding mechanism of the Hippo pathway transcription factor TEAD4. *Oncogene.* 36:4362–4369. https://doi.org/10.1038/onc.2017.24

Shinobu, N., T. Iwamura, M. Yoneyama, K. Yamaguchi, W. Suhara, Y. Fukuhara, F. Amano, and T. Fujita. 2002. Involvement of TIRAP/MAL in signaling for the activation of interferon regulatory factor 3 by lipopolysaccharide. *FEBS Lett.* 517:251–256. https://doi.org/10.1016/S0014-5793(02)02636-4

Steinhardt, A.A., M.F. Gayyed, A.P. Klein, J. Dong, A. Maitra, D. Pan, E.A. Montgomery, and R.A. Anders. 2008. Expression of Yes-associated protein in common solid tumors. *Hum. Pathol.* 39:1582–1589. https://doi.org/10.1016/j.humpath.2008.04.012

Wang, S., F. Xie, F. Chu, Z. Zhang, B. Yang, T. Dai, L. Gao, L. Wang, L. Ling, J. Jia, et al. 2017. YAP antagonizes innate antiviral immunity and is targeted for lysosomal degradation through IKKε-mediated phosphorylation. *Nat. Immunol.* 18:733–743. https://doi.org/10.1038/ni.3744

Wu, J., and Z.J. Chen. 2014. Innate immune sensing and signaling of cytosolic nucleic acids. *Annu. Rev. Immunol.* 32:461–488. https://doi.org/10.1146/annurev-immunol-032713-120156

Wu, S., Y. Liu, Y. Zheng, J. Dong, and D. Pan. 2008. The TEAD/TEF family protein Scalloped mediates transcriptional output of the Hippo growth-regulatory pathway. *Dev. Cell.* 14:388–398. https://doi.org/10.1016/j.devcel.2008.01.007

Yoneyama, M., W. Suhara, and T. Fujita. 2002. Control of IRF-3 activation by phosphorylation. *J. Interferon Cytokine Res.* 22:73–76. https://doi.org/10.1089/107999002753452674

Zanconato, F., M. Forcato, G. Battilana, L. Azzolin, E. Quaranta, B. Bodega, A. Rosato, S. Bicciato, M. Cordenonsi, and S. Piccolo. 2015. Genome-wide association between YAP/TAZ/TEAD and AP-1 at enhancers drives oncogenic growth. *Nat. Cell Biol.* 17:1218–1227. https://doi.org/10.1038/ncb3216

Zeng, Q., and W. Hong. 2008. The emerging role of the hippo pathway in cell contact inhibition, organ size control, and cancer development in mammals. *Cancer Cell.* 13:188–192. https://doi.org/10.1016/j.ccr.2008.02.011

Zhang, H., C.Y. Liu, Z.Y. Zha, B. Zhao, J. Yao, S. Zhao, Y. Xiong, Q.Y. Lei, and K.L. Guan. 2009. TEAD transcription factors mediate the function of TAZ in cell growth and epithelial-mesenchymal transition. *J. Biol. Chem.* 284:13355–13362. https://doi.org/10.1074/jbc.M900843200

Zhang, L., F. Ren, Q. Zhang, Y. Chen, B. Wang, and J. Jiang. 2008a. The TEAD/TEF family of transcription factor Scalloped mediates Hippo signaling in organ size control. *Dev. Cell.* 14:377–387. https://doi.org/10.1016/j.devcel.2008.01.006

Zhang, Q., F. Meng, S. Chen, S.W. Plouffe, S. Wu, S. Liu, X. Li, R. Zhou, J. Wang, B. Zhao, et al. 2017. Hippo signalling governs cytosolic nucleic acid sensing through YAP/TAZ-mediated TBK1 blockade. *Nat. Cell Biol.* 19:362–374. https://doi.org/10.1038/ncb3496

Zhang, W., Y. Gao, P. Li, Z. Shi, T. Guo, F. Li, X. Han, Y. Feng, C. Zheng, Z. Wang, et al. 2014. VGLL4 functions as a new tumor suppressor in lung cancer by negatively regulating the YAP-TEAD transcriptional complex. *Cell Res.* 24:331–343. https://doi.org/10.1038/cr.2014.10

Zhang, Y., T. Liu, C.A. Meyer, J. Eeckhoute, D.S. Johnson, B.E. Bernstein, C. Nusbaum, R.M. Myers, M. Brown, W. Li, and X.S. Liu. 2008b. Model-based analysis of ChIP-Seq (MACS). *Genome Biol.* 9:R137. https://doi.org/10.1186/gb-2008-9-9-r137

Zhao, B., X. Wei, W. Li, R.S. Udan, Q. Yang, J. Kim, J. Xie, T. Ikenoue, J. Yu, L. Li, et al. 2007. Inactivation of YAP oncoprotein by the Hippo pathway is involved in cell contact inhibition and tissue growth control. *Genes Dev.* 21:2747–2761. https://doi.org/10.1101/gad.1602907

Zhao, B., X. Ye, J. Yu, L. Li, W. Li, S. Li, J. Yu, J.D. Lin, C.Y. Wang, A.M. Chinnaiyan, et al. 2008. TEAD mediates YAP-dependent gene induction and growth control. *Genes Dev.* 22:1962–1971. https://doi.org/10.1101/gad.1664408

Zhao, B., L. Li, Q. Lei, and K.L. Guan. 2010. The Hippo-YAP pathway in organ size control and tumorigenesis: An updated version. *Genes Dev.* 24:862–874. https://doi.org/10.1101/gad.1909210